Chemical Engineering Journal 520 (2025) 166241

Contents lists available at ScienceDirect

Chemical Engineering Journal

journal homepage: www.elsevier.com/locate/cej

Directional synthesis of high-density aviation fuel through CO_2 hydrogenation coupling with naphthalene alkylation over $ZnZrO_x$/Hβ catalyst

Xiaopo Niu [a], Hongming Qian [a], Dongyuan Cai [a], Wenli Zhao [b], Qingfa Wang [b], Quanli Ke [a], Guokai Cui [a], Chunliang Ge [c], Lina Tang [c,*], Hanfeng Lu [a,*]

[a] Institute of Catalytic Reaction Engineering, College of Chemical Engineering, Zhejiang University of Technology, Hangzhou 310014, PR China
[b] Key Laboratory for Green Chemical Technology of Ministry of Education, School of Chemical Engineering and Technology, Tianjin University, Tianjin 300072, PR China
[c] Zhejiang Zheneng Technology & Environment Group Co., Ltd., Zhejiang Provincial Energy Group Co. Ltd., Hangzhou 310012, PR China

ARTICLE INFO

Keywords:
High-density aviation fuel
Alkylated polycyclic hydrocarbons
Coupling conversion
Bifunctional catalyst
CO_2 utilization

ABSTRACT

Hydrogenation of CO_2 and green H_2 into sustainable high-density aviation fuels is a crucial route to satisfy the high-performance fuel demands of advanced aircrafts and facilitate carbon neutrality in the aviation industry, whereas existing technologies mainly produce low-energy-density components. Herein, coupling CO_2 hydrogenation with polyaromatic alkylation is proposed to synthesize alkylated polycyclic hydrocarbons with high energy density and superior low-temperature property. The effect of electronic interactions in the $ZnZrO_x$/Hβ catalysts prepared utilizing oxalate-mediated precipitation strategy on the coupling reaction of CO_2 hydrogenation and naphthalene alkylation was proverbially investigated. Appropriate Zn incorporation is beneficial to boost the electronic action within $ZnZrO_x$ solid solutions and generate abundant electron-rich Zn species and oxygen defects, thereby promoting the production of more methoxy intermediate derived from CO_2 hydrogenation for the alkylation with naphthalene. The $ZnZrO_x$/Hβ catalyst with molar ratio of 1:8 showed the optimal space time yield of 5.9 μmol·g-1 oxide·s^{-1} and selectivity of 86.4 % for alkylnaphthalene at 360 °C under 4 MPa. Moreover, it also presented exceptional long-term catalytic stability over a 100 h on stream, exhibiting outstanding industrial application prospects. In situ DRIFTS and DFT simulations showed that CO_2 preferentially formed *H_3CO by formate route in $ZnZrO_x$ and then diffused to Hβ zeolite for alkylation, establishing a coupled transformation pathway for the preparation of alkylnaphthalene. After blending with JP-10, the high-density aviation fuel with superb density of 0.949 g·mL^{-1} was obtained, which also illustrated higher oxidation onset temperature of 219.6 °C and shorter ignition delay time of 2276 ms, providing a novel pathway and theoretical foundation for the directional synthesis of sustainable high-density aviation fuels.

1. Introduction

High-density aviation fuel, a critical component of liquid propellants, is featured by high density (≥0.85 g·mL^{-1}), superior volumetric net heat of combustion and low freezing point, serving as strategic energy resource vital for safeguarding national aviation security [1–3]. With the increasing exhaustion of fossil fuels and under the strategic goals of carbon peaking and carbon neutrality, it is imperative to exploit sustainable high-density aviation fuels. The International Air Transport Association (IATA) anticipates that the adhibition of sustainable aviation fuel will contribute approximately 65 % toward achieving net-zero emissions target in the aviation industry by 2050 [4]. Currently, the manufacturing technologies principally include hydroprocessed esters and fatty acids (HEFA), gasification Fischer-Tropsch synthesis (FT), alcohol to jet fuel (ATJ) and power to liquid (PTL) [5,6]. Mindfully, the PTL process on the basis of CO_2 coupled with green H_2 can realize carbon reduction of up to 99 % and is not restricted by feedstock availability, making it a critical route for attaining net-zero emissions while simultaneously addressing the stringent requirement for high-density aviation fuels driven by the advancement of modern

* Corresponding authors.
E-mail addresses: linatang0225@163.com (L. Tang), luhf@zjut.edu.cn (H. Lu).

https://doi.org/10.1016/j.cej.2025.166241
Received 15 April 2025; Received in revised form 26 June 2025; Accepted 19 July 2025
Available online 22 July 2025

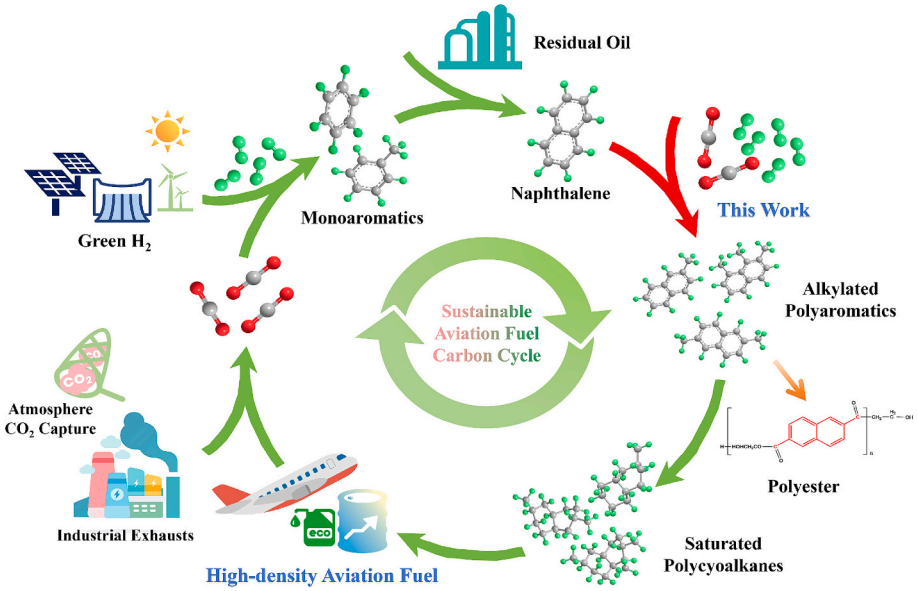

Fig. 1. Production of sustainable high-density aviation fuel and carbon cycle based on CO_2 hydrogenation coupling with naphthalene alkylation.

aircraft [7].

Due to the inherently low reactivity of CO_2, complex hydrogenation kinetics and rigorous energy barrier associated with C—C coupling, the hydrogenation reactions proceed tardily and preferentially generate C_1 molecules [8–13]. Recently, Yao et al. [9] reported Fe-Mn-K catalysts to couple CO_2 with green H_2 for the synthesis of aviation fuel, accomplishing the selectivity of 47.8 % for C_8-C_{16} linear hydrocarbons. For the sake of reinforcing the yield of cyclic compounds, Arslan et al. [14] developed $ZnCr_2O_4$/Sbx-HZSM-5 catalyst, which promoted the selective to monoaromatics (>80 %) in aviation fuels synthesized via CO_2 hydrogenation. Nevertheless, aviation fuels manufactured through existing technologies principally comprise C_8-C_{16} linear alkanes and monocyclic substances, demonstrating relatively low energy density (≤0.78 $g{\cdot}mL^{-1}$), which is difficult to meet the requirements of advanced aerospace vehicles for fuels with high energy density (≥0.85 $g{\cdot}mL^{-1}$). In consequence, it remains highly challenging to yield aviation fuels that synchronously possess high energy density and splendid low-temperature performances [15]. Fortunately, alkylnaphthalene and its hydrosaturated derivatives unite both high energy density and favorable low temperature parameters, and are therefore widely utilized in the preparation of high-density aviation fuels [16,17]. Accordingly, designing applicable pathways and establishing high-performance catalysts to strengthen the selectivity toward alkylated polycyclic hydrocarbons is pivotal for transforming CO_2 into high-density aviation fuels possessing superior energy density and excellent low-temperature properties.

Residue oil is lavish in polyaromatics such as naphthalene and phenanthrene, which have carbon number consistent with those of aviation fuels and possess high energy density, yet their inferior low-temperature properties and tendency to form carbon deposits during combustion limit the application in high-density fuels [18,19]. Thrillingly, the introduction of alkyl substituents can improve the low-temperature property and promote complete combustion. Based on this, coupling CO_2 hydrogenation with the alkylation of polyaromatics enables the precise synthesis of alkylated polyaromatics, the key components of high-density aviation fuels. Fig. 1 depicts the production of sustainable high-density aviation fuel and carbon cycle in the light of CO_2 hydrogenation coupling with naphthalene alkylation. This strategy not only contributes to prominent carbon emission slash but also strengthens the high-value utilization of residue oil. Metal oxides with redox properties can realize the hydrogenation of CO_2 to methoxy ($*H_3CO$), whereas acidic zeolites are in charge of the activation of polyaromatics for alkylation, ultimately harvesting alkylated polycyclic hydrocarbons [20]. Thereinto, the generation of $*H_3CO$ from CO_2 is an exothermic process (-45.9 $kJ{\cdot}mol^{-1}$), typically conducted below 300 °C, while alkylation of polyaromatics requires higher temperatures (>350 °C) [21–23]. Thus, settling the thermal compatibility between these reactions delegates a critical challenge for achieving efficient coupling. As reported, $ZnZrO_x$ has shown superior CO_2 hydrogenation activity and can attain notable methanol selectivity at 320 °C [24–27]. Moreover, Hβ zeolite with three-dimensional 12-membered ring porous architectures, tunable acidity and high specific surface area offers an ideal platform for alkylation [28]. Fabricating $ZnZrO_x$/Hβ catalysts is anticipated to the one of the most promising tactics for coupling CO_2 hydrogenation with polyaromatics alkylation to produce alkylated polyaromatics, which serve as the crucial components of high-density aviation fuels. Expressly, the activation of CO_2 on $ZnZrO_x$ is of great importance for the coupling procedure. Coprecipitation is commonly used for synthesizing $ZnZrO_x$ solid solutions, however, the $ZnZrO_x$ obtained utilizing ammonium carbonate as precipitant typically owns limited oxygen vacancies, claiming that the further consolidation of catalytic activities is desired [29]. Attentively, the electronic interactions in $ZnZrO_x$ have not been extensively revealed, hindering the efficient implementation of catalytic hydrogenation coupling reactions.

In this work, catalytic coupling CO_2 hydrogenation with naphthalene alkylation is proposed for the directional synthesis of alkylnaphthalenes, an essential components of high-density aviation fuel with superior fuel properties. A series of $ZnZrO_x$/Hβ catalysts with various Zn:Zr molar ratios were fabricated employing oxalate-mediated coprecipitation method to elucidate the influence of electronic interaction on the catalytic performance. Comprehensive experiments clarified that an optimal doping of Zn intensified electronic perturbation and synergistic action between Zn and Zr within the $ZnZrO_x$ solid solutions, promoting the formation of oxygen vacancies. The $ZnZrO_x$/Hβ catalyst with the ratio of 1:8 reached the supreme space time yield for coupling alkylation (STY_{ALK} = 5.9 μmol·g-1 oxide·s^{-1}) and an eminent selectivity of 86.4 % to alkylnaphthalenes. Besides, the coupling mechanisms were further illustrated through in situ DRIFTS and DFT simulations. Excitedly, the synthesized fuel components were employed as additives to JP-10 fuel, significantly improving the density and thermal stability as well as shorter ignition delay time.

2. Experimental section

2.1. Catalyst synthesis

A series of $ZnZrO_x$ solid solutions with various Zn:Zr molar ratios ranging from 1:4 to 1:16 were synthesized via an oxalate-mediated coprecipitation strategy. Taking the preparation of $ZnZrO_x$ with a Zn:Zr ratio of 1:8 as an example, 0.50 g $Zn(NO_3)_2{\cdot}6H_2O$ (99 %, Aladdin) and 5.74 g $Zr(NO_3)_4{\cdot}5H_2O$ (99 %, Macklin) were dissolved in 150 mL anhydrous ethanol (99.9 %, Adamas-beta). Subsequently, 50 mL ethanol solution containing 3.07 g oxalic acid (99 %, Aladdin) was added dropwise into the above solution at a rate of 2.5 $mL{\cdot}min^{-1}$ under ambient temperature with vigorous stirring. Following the addition, the mixture was stirred continuously for another 2 h. Then, the resulting precipitate was collected by centrifugation, washed thoroughly three times with ethanol, dried at 110 °C, ground and calcined at 500 °C for 6 h with a heating rate of 5 $°C{\cdot}min^{-1}$. Finally, the obtained samples were denoted as $Zn_1Zr_4O_x$, $Zn_1Zr_6O_x$, $Zn_1Zr_8O_x$, $Zn_1Zr_{12}O_x$ and $Zn_1Zr_{16}O_x$, respectively. The composite $ZnZrO_x$/Hβ catalysts with varying intimacies were fabricated utilizing two different integration approaches. One was acquired by grinding-mixing (GM), in which a predetermined mass of $ZnZrO_x$ solid solution and Hβ zeolite ($SiO_2/Al_2O_3 = 25$, Clariant) were ground together in an agate mortar for 15 min. The other was synthesized through co-precipitation (CR), where Hβ was introduced into the alcoholic solution prior to the dropwise addition of oxalic acid. The resulting catalysts were labeled as $ZnZrO_x$/Hβ (GM) and $ZnZrO_x$/Hβ (CR), respectively. Unless otherwise specified, the $ZnZrO_x$/Hβ catalysts employed in this work denote those prepared via the GM method.

2.2. Catalyst characterization

X-ray diffraction (XRD) analyses were carried out on a Rigaku smartlab diffractometer utilizing a Ni-filtered Cu Kα radiation source at 40 kV and 150 mA over the 2θ range of 20–90°. The interplanar spacing of the $ZnZrO_x$(101) facet was calculated according to the Bragg Eq. (1) [30].

$$2d\sin\theta = n\lambda \tag{1}$$

where d, θ, n, and λ are the interplanar spacing, diffraction angle, diffraction order (typically $n = 1$) and wavelength of radiation source (0.15406 nm), respectively.

The textural properties of synthesized samples were measured via using a Micromeritics 3FLEX analyzer at liquid N_2 temperature. Prior to the measurement, the samples were degassed at 300 °C for 12 h under vacuum. Moreover, the morphologies and elemental distributions were examined utilizing transmission electron microscopy (TEM), high resolution TEM (HRTEM), high-angle annular dark-field scanning transmission electron microscopy (HAADF-STEM) and elemental mapping performed on a FEI Tecnai G2 F30 facility. Quasi in situ X-ray photoelectron spectroscopy (XPS) was executed employing a Thermo Fisher ESCALAB-250XI instrument. Meanwhile, all catalysts were reduced at 350 °C for 2.5 h under a flowing 10 % H_2/N_2 gas prior to the measurements, and the binding energies were calibrated against the C1s peak at 284.8 eV. Electron paramagnetic resonance (EPR) was carried out using a Bruker EMXplus-6/1 device at room temperature.

Temperature programmed reduction of H_2 (H_2-TPR), temperature programmed desorption of H_2 (H_2-TPD) and CO_2 (CO_2-TPD) were performed on a VDsorb-91i facility. For H_2-TPR tests, 150 mg of sample was placed into the U-shaped quartz tube and evacuated at 300 °C for 1 h in flowing He of 30 $mL{\cdot}min^{-1}$. Afterwards, the sample was cooled to 50 °C and 10 % of H_2/Ar was introduced. Next, the tube was heated to 900 °C with a heating rate of 10 $°C{\cdot}min^{-1}$ and the reduction signals were recorded by a thermal conductivity detector (TCD). In H_2-TPD and CO_2-TPD experiments, 150 mg of sample was pretreated at 350 °C for 2 h by 10 % H_2/Ar. After cooling to 50 °C, the sample was saturated with H_2 or CO_2. Subsequently, the physically adsorbed gas molecules were eliminated in He with flowing rate of 30 $mL{\cdot}min^{-1}$. The desorption profiles were conducted at 50–900 °C (10 $°C{\cdot}min^{-1}$) and collected by TCD under He flow. The H_2-D_2 exchange measurements were performed in a downflow fixed-bed reactor. In a typical run, 100 mg of catalyst was initially reduced at 350 °C for 2 h in 10 % H_2/N_2 gas flow. After cooling down to room temperature, the gas flow was switched to 5 % D_2/5 % H_2/N_2, and the baseline was waited to stabilize. Then, the H_2-D_2 exchange reactions were implemented in the temperature range of 30–300 °C, and the mass signals were continuously monitored using an OMNI Star™ Gas Analysis System.

In situ diffuse reflectance infrared Fourier transforms spectroscopy (DRIFTS) were executed by utilizing a Bruker VERTEX 70v spectrometer with a mercury cadmium telluride (MCT) detector. The catalyst was loaded into an in situ Harrick cell and pretreated by 10 % H_2/N_2 flow at 350 °C for 2 h. Thereafter, the catalyst was purged with N_2 for 1 h and cooled to the target temperature of 320 °C. At the same time, the background spectrum was collected in flowing N_2 of 30 $mL{\cdot}min^{-1}$ under 0.2 MPa. Posteriorly, the mixture gas (CO_2:H_2:N_2 = 23:69:8) was imported into the in situ cell, and concurrently the MCT was used to record the spectra for 75 min over 64 scans at a resolution of 4 cm^{-1}. At last, the inlet gas was changed to 10 % H_2/N_2 for additional 75 min to investigate the hydrogenation stage.

2.3. Catalytic evaluation

The catalytic performance evaluations of series $ZnZrO_x$/Hβ catalysts were conducted in a fixed-bed microreactor equipped with a quartz-lined stainless reactor tube (ID: 7 mm, length: 800 mm) and manufactured by Quzhou Vodo Instrument Co., Ltd. Classically, 1 g of composite catalyst was diluted to 3 mL with quartz sand and then placed into the central region of reactor tube. A thermocouple was fixed in the center of catalyst bed to monitor the actual temperature. The CO_2 hydrogenation coupling with naphthalene reaction was initiated after the activation procedure where the catalyst was reduced at 350 °C for 2 h under an atmosphere of 10 % H_2/N_2 with a flowing rate of 100 $mL{\cdot}min^{-1}$. Afterwards, the gaseous mixture of CO_2:H_2:N_2 (23:69:8) was introduced into the reactor and pressurized to 4 MPa. Subsequently, a liquid feedstock of 5 wt% naphthalene in cyclohexane was injected utilizing a plunger pump. Regularly, the coupling reaction conducted at 320–400 °C and 4 MPa with a gas hourly space velocity (GHSV) of 6000 mL·g-1 $cat{\cdot}h^{-1}$ and a weight hourly space velocity (WHSV) of 8.5 h^{-1}. After the reactions, gaseous samples were analyzed online using an Agilent 8890 gas chromatograph (GC) equipped with TCD and flame ionization detector (FID). Moreover, the liquid products were analyzed offline by 8890 GC after gas-liquid separation.

The conversions of CO_2 (X_{CO2}) and naphthalene (X_{C10H8}) were calculated according to formulas (2) and (3), respectively.

$$X_{CO_2} = \frac{CO_{2_{inlet}} - CO_{2_{outlet}}}{CO_{2_{inlet}}} \times 100\% \tag{2}$$

$$X_{C_{10}H_8} = \frac{C_{10}H_{8_{inlet}} - C_{10}H_{8_{outlet}}}{C_{10}H_{8_{inlet}}} \times 100\% \tag{3}$$

where CO_{2inlet} and $CO_{2outlet}$ are the molar amounts of CO_2 at the inlet and outlet, respectively, while $C_{10}H_{8inlet}$ and $C_{10}H_{8outlet}$ denote the molar quantities of naphthalene at the inlet and outlet, respectively.

The liquid production distributions (S) were determined by Eq. (4).

$$S_{C_nH_m} = \frac{C_nH_{m_{outlet}}}{\sum_6^n C_nH_{m_{outlet}} - C_{10}H_{8_{outlet}}} \times 100\% \tag{4}$$

where $C_nH_{moutlet}$ represents the molar amount of a specific compound in the liquid product.

The carbon usages of CO_2 were classified into four pathways: CO (U_{CO}), dimethyl ether (U_{DME}), C1-C5 hydrocarbons ($U_{C1\text{-}C5}$) and

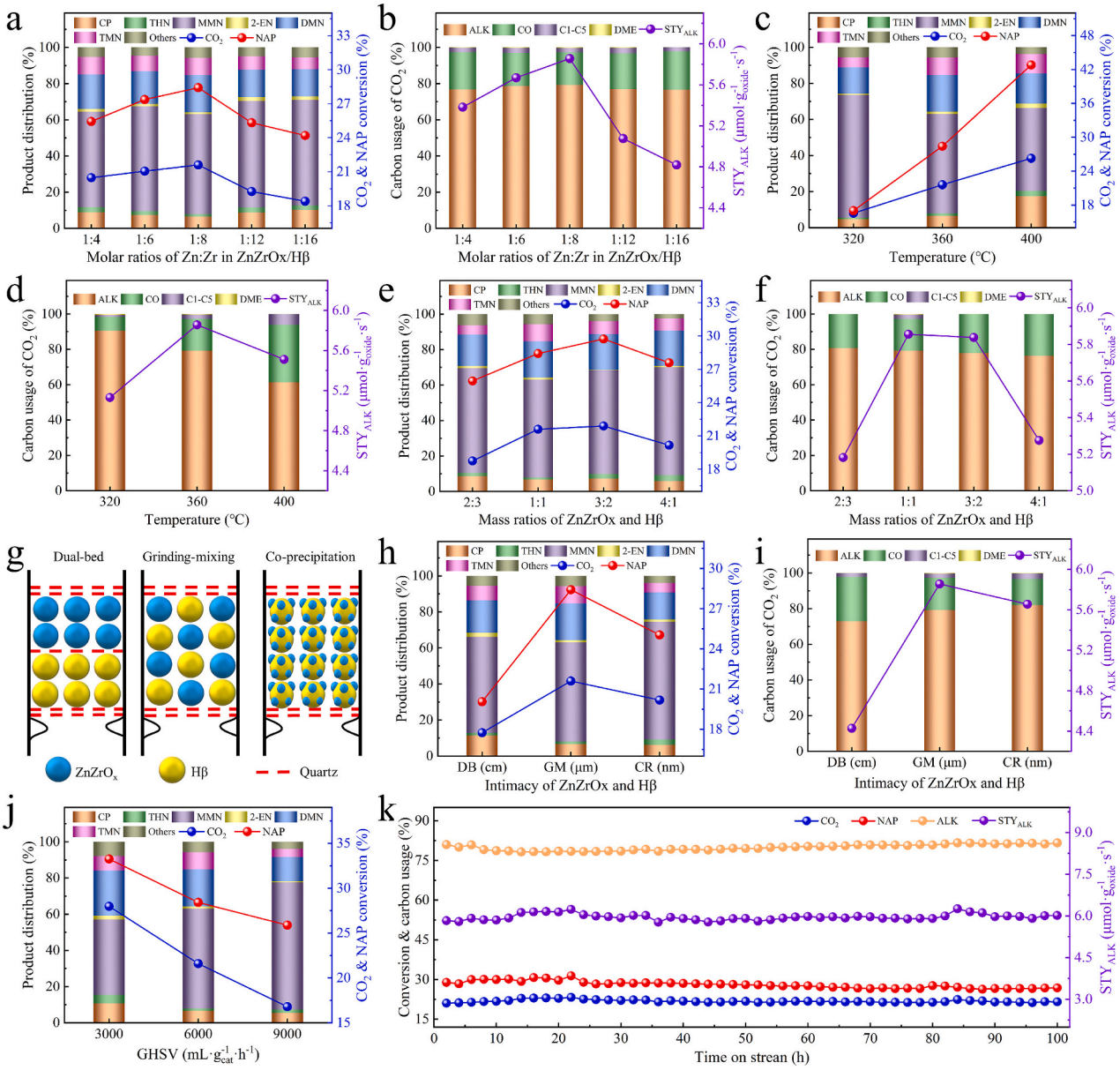

Fig. 2. Catalytic performance of $ZnZrO_x$/Hβ catalysts for CO_2 hydrogenation coupling with NAP alkylation. The influence of molar ratios of Zn:Zr in $ZnZrO_x$/Hβ catalysts: (a) product distribution and conversion, (b) carbon usage of CO_2 and STY_{ALK} normalized to oxide mass. Standard reaction conditions: 4 MPa, 360 °C, GHSV of mixture gas (CO_2:H_2:N_2 = 23:69:8) = 6000 mL·g-1 cat·h^{-1}, WHSV of NAP solution = 9.5 h^{-1}. (c, d) The effect of reaction temperature on the catalytic activities of $Zn_1Zr_8O_x$/Hβ catalyst. (e, f) Comparison of the activities of $Zn_1Zr_8O_x$/Hβ catalyst with diverse mass ratios of $ZnZrO_x$ and Hβ. The effect of intimacy between $ZnZrO_x$ and Hβ zeolite on the catalytic performances of $Zn_1Zr_8O_x$/Hβ catalyst: (g) schematic of mixing modes of dual-bed (DB), grinding-mixing (GM) and co-precipitation (CR), (h) product distribution and conversion, (i) carbon usage of CO_2 and STY_{ALK} normalized to oxide mass. (j) The impact of GHSV on the catalytic performances of $Zn_1Zr_8O_x$/Hβ catalyst. (k) Stability evaluation of $Zn_1Zr_8O_x$/Hβ catalyst. (NAP: naphthalene, CP: cracking products, THN: tetrahydronaphthalene, MMN: monomethylnaphthalene, 2-EN: 2-ethylnaphthalene, DMN: dimethylnaphthalene, TMN: trimethylnaphthalene, Others: other products).

coupling alkylation (U_{ALK}), which were calculated on the basis of formulas (5)–(8).

$$U_{CO} = \frac{CO_{outlet}}{\sum_{10}^{n}(n-10)C_nH_{m_{outlet}} + \sum_{1}^{5} nC_nH_{m_{outlet}} + MeOH + 2DME + CO_{outlet}} \times 100\% \quad (5)$$

$$U_{DME} = \frac{2DME}{\sum_{10}^{n}(n-10)C_nH_{m_{outlet}} + \sum_{1}^{5} nC_nH_{m_{outlet}} + MeOH + 2DME + CO_{outlet}} \times 100\% \quad (6)$$

$$U_{C1-C5} = \frac{\sum_{1}^{5} nC_nH_{m_{outlet}}}{\sum_{10}^{n}(n-10)C_nH_{m_{outlet}} + \sum_{1}^{5} nC_nH_{m_{outlet}} + MeOH + 2DME + CO_{outlet}} \times 100\% \quad (7)$$

$$U_{ALK} = \frac{\sum_{10}^{n}(n-10)C_nH_{m_{outlet}}}{\sum_{10}^{n}(n-10)C_nH_{m_{outlet}} + \sum_{1}^{5} nC_nH_{m_{outlet}} + MeOH + 2DME + CO_{outlet}} \times 100\% \quad (8)$$

The space time yield (STY) of alkylnaphthalene, based on carbon atoms derived from CO_2 and normalized to $ZnZrO_x$ weight was analyzed based on Eq. (9).

$$STY_{ALK}\left(mg{\cdot}g_{oxide}^{-1}{\cdot}h^{-1}\right) = \frac{X_{CO_2} \times GHSV_{CO_2} \times U_{ALK}}{22.4 \times m_{oxide}} \quad (9)$$

where $GHSV_{CO2}$ refers to the flow rate of CO_2 per gram of catalyst per hour, and m_{oxide} is allotted to the mass ratio of oxide in composite catalyst.

2.4. Computational detail

All spin-polarized density functional theory (DFT) calculations were implemented by the Vienna Ab-initio Simulation Package (VASP) software. Exchange-correlation interactions were treated with the general gradient approximation (GGA) using the Perdew-Burke-Ernzerhof (PBE) functional. The interactions between valence electron and nucleuses were described utilizing the projector augmented wave (PAW) method, and the cutoff energy was set to 450 eV. Dispersion interactions were corrected employing DFT-D4 method [31–33]. To account for the on-site Coulomb interactions of the strongly localized Zr 4d electrons, the DFT + U approach was adopted with a Hubbard parameter (U–J) of 4.0 eV [34]. A vacuum layer of 15 Å was appended along the z-axis to avoid the influence of periodicity. The convergence thresholds for energy and force were 10^{-6} eV and 0.05 eV/Å, respectively, and the Brillouin zone integration was sampled using Monkhorst-Pack *k*-points (2 × 2 × 1) mesh. Geometry optimizations were performed using the conjugate gradient strategy. Transition states were located by the combination of the climbing image nudged elastic band (CINEB) and dimer methods, and were further verified through frequency analysis, guaranteeing the being of only one imaginary frequency. Besides, the DFT data were managed using VASPKIT software [35]. The adsorption energy (△E) was calculated as formula (10).

$$\Delta E = E_{total} - E_{slab} - E_{ads} \quad (10)$$

where E_{total} represents the total energy of the adsorption system, E_{slab} is the energy of the isolated slab, and $E_{ads.}$ is the energy of the adsorbed molecule.

2.5. Fuel properties measurement

A Mettler Toledo DE40 density meter was utilized to determine the density of prepared aviation fuels in accordance with the ASTM D4052 standard [36]. Thermal stability was tested using pressure differential scanning calorimetry (PDSC) on a NETZSCH DSC 204 HP facility following the ASTM E2009 [37]. Approximately 10 mg of the sample was placed in an aluminum crucible, sealed in the sample chamber, and pressurized to 3500 kPa. The experiments were carried out at 50–300 °C with a heating rate of 10 °C·min^{-1} under a flowing air of 50 mL·min^{-1}. The oxidation onset temperature was calculated via the intersection between the extrapolated baseline and the tangent to the maximal exothermic peak. In addition, combustion quality and ignition delay time were evaluated in a hot-plate ignition equipment. The hot-plate

was heated to 450 °C, and a 12 μL of fuel droplet was dropped. The combustion process was recorded using FASTCAM UX50-type 160 K-CGB high-speed camera. Ignition delay time was defined as the interval between the occurrence of the flame and the initial fuel droplet contacting the hot-plate.

3. Results and discussion

3.1. Catalytic performance of directional synthesis of high-density aviation fuel

The directional synthesis of high-density aviation fuels over $ZnZrO_x$/Hβ catalysts was performed in a fixed-bed microreactor based on CO_2 hydrogenation coupling with naphthalene (NAP) alkylation at temperature ranging from 320 °C to 400 °C under pressure of 4 MPa. The catalytic activities over the $ZnZrO_x$ samples prepared using oxalic acid (OA) and ammonium carbonate (AC) as precipitants were first performed. As depicted in Fig. S1, the $ZnZrO_x$/Hβ(OA) exhibited better CO_2 conversion in the coupling reaction compared to the $ZnZrO_x$/Hβ(AC) catalyst under identical reaction condition, which was ascribed to the abundant defects existed in the $ZnZrO_x$(OA) oxides (detailed analyses are provided in the Section 3.2). Therefore, the oxalate-mediated coprecipitation strategy was employed for synthesizing $ZnZrO_x$/Hβ catalysts to enable highly efficient coupling between CO_2 hydrogenation and NAP alkylation.

3.1.1. Comparison of catalytic activities of $ZnZrO_x$/Hβ with diverse Zn:Zr molar ratios

First of all, the impact of Zn incorporation amount on the coupling performances was extensively investigated. As exhibited in Fig. 2a, the conversions for CO_2 and NAP initially magnified and then decreased with the Zn:Zr molar ratio elevating from 1:4 to 1:16, exhibiting a peak at the ratio of 1:8. In the meantime, the maximum conversion of 21.6 % for CO_2 and 28.4 % for NAP were attained over $Zn_1Zr_8O_x$/Hβ catalyst, indicating the existence of synergistic interaction in $ZnZrO_x$. Tuning Zn doping content can regulate the distribution of active sites in $ZnZrO_x$, thereby affecting the catalytic activities between CO_2 hydrogenation and NAP alkylation. Besides, all the $ZnZrO_x$/Hβ catalysts with different Zn:Zr molar ratios demonstrated outstanding selectivity (> 81.5 %) toward alkylnaphthalenes (ANs). Of which monomethylnaphthalene (MMN), dimethylnaphthalene (DMN) and trimethylnaphthalene (TMN) were dominating, along with a minor amount of 2-ethylnaphthalene (2-EN). These substances are terrific high-density aviation fuel components with superb volumetric net heat of combustion and superior low-temperature properties, indicating that coupling CO_2 hydrogenation and NAP alkylation can accomplish highly selective and directional synthesis of high-density aviation fuels. In addition, a handful of cracking products (CP) and tetrahydronaphthalene (THN) were also detected in the liquid due to the strong acidity of Hβ zeolite. In particular, the selectivity to MMN, DMN, 2-EN and TMN on the $Zn_1Zr_4O_x$/Hβ catalyst were 52.6 %, 19.0 %, 1.6 % and 9.8 % respectively. When the Zn:Zr ratio increased to 1:6, the selectivity to MMN heightened to 57.8 %, which could be attributed to the higher CO_2 conversion leading to the formation of more methyl active intermediates that undergo alkylation with NAP. For $Zn_1Zr_8O_x$/Hβ catalyst, the selectivity to MMN declined to 55.2 %, while the selectivity to DMN increased to 20.4 %, demonstrating that the continuous alkylation reaction was strengthened. However, further improving Zn:Zr ratio to 1:16, the selectivity to DMN and TMN decreased, coupled with an increase in MMN. This was in line with the variation tendency of CO_2 conversion. Hence, it could be concluded that higher CO_2 conversion produced luxuriant methyl intermediates, which then diffused to Hβ zeolite for alkylation. This not only accelerated the transformation of reactants but also strengthened the selectivity to polymethyl substituted NAP. In addition, the carbon usage for CO_2 in the coupling process was also calculated and is depicted in Fig. 2b. The $ZnZrO_x$/Hβ catalyst showed the supreme alkylation selectivity of 79.2 % at the molar ratio of 1:8, indicating the efficient coupling of CO_2 hydrogenation with NAP alkylation and thus reinforcing the synthesis of high-density aviation fuel components. In parallel, a markedly superior STY_{ALK} of 5.9 μmol·g-1 oxide·s^{-1} was also obtained over the $Zn_1Zr_8O_x$/Hβ catalyst, confirming its ascendant coupling efficiency. Consequently, the Zn:Zr ratio of 1:8 is considered the applicable composition, at which Zn and Zr presented wonderful synergistic interaction in the $ZnZrO_x$/Hβ catalytic system.

3.1.2. Influence of reaction temperature on the coupling activities

On account of the above experiments, $Zn_1Zr_8O_x$/Hβ exhibited the best catalytic performance and was thus chosen as the primary subject for further investigation. CO_2 hydrogenation is an exothermic reaction [38], while the alkylation for NAP is an endothermic process [23,39], so reaction temperature plays a crucial factor in governing the coupling efficiency. With the temperature rising up from 320 °C to 400 °C, the conversions of CO_2 and NAP substantially improved from 16.6 % to 26.3 % and from 17.0 % to 42.8 %, respectively (Fig. 2c). However, the selectivity of ANs (MMN, DMN, TMN and 2-EN) decreased continuously from 88.9 % to 76.0 %, which could be ascribed to the attenuated carbon usage of CO_2 into the alkylation owing to the grievous reverse water gas shift (RWGS) reaction and intensive cracking process of NAP. At 320 °C, $Zn_1Zr_8O_x$/Hβ showed the highest MMN selectivity of 68.0 % as well as the lowest selectivity to DMN (14.5 %) and TMN (5.6 %). In addition, the selectivity of MMN reduced to 55.2 % as the temperature increased to 360 °C, while the selectivity to DMN and TMN increased to 20.4 % and 9.6 % respectively, suggesting the occurrence of successive alkylation processes. Nevertheless, a further temperature rise to 400 °C led to a significant decline in both MMN and DMN, whereas the selectivity for CP risen to 17.5 %, meaning that excessive temperature mainly boosted the cracking of NAP, which was detrimental to the coupling performance. The carbon usage data in Fig. 2d also illustrated that with rising reaction temperature, the alkylation activity degraded from 90.5 % to 61.3 %. Simultaneously, the utilization pathway of CO enlarged from 7.7 % to 32.6 %. Moreover, an 86.4 % selectivity of ANs was acquired at 360 °C. Owing to the relatively fine match of catalytic activity and coupling property, the highest STY_{ALK} value was also obtained at the same time. Additionally, Fig. S2-S5 exhibits the detailed activities data for the coupling reaction over the other $ZnZrO_x$/Hβ catalysts with different Zn:Zr molar ratios, which also demonstrated analogical catalytic properties with various temperature.

3.1.3. Effect of synergy between metal oxides and zeolite on the reaction natures

The $ZnZrO_x$ solid solution can be used to transform CO_2 and H_2 into methoxy species, while Hβ zeolite is responsible for the alkylation of NAP with methoxy [39–42]. Thus, the mass ratios of oxides and zeolite are of vital importance for the coupling conversion, as it determines the synergy between the active sites for CO_2 and NAP activation. As elucidated in Fig. 2e, with the increase of $Zn_1Zr_8O_x$ ratio in composite catalyst, a volcano-shaped relationship was found in the CO_2 and NAP conversions, while the selectivity to ANs remained relatively constant in the range of 83.2–88.3 %. When the mass ratio was 3:2, the highest conversions for CO_2 (21.9 %) and NAP (29.7 %) were acquired, which were 0.3 % and 1.3 % higher respectively, than those gained on the mass ratio of 1:1. Concurrently, the ANs selectivity of 86.0 % was delivered. Nevertheless, the carbon usage for alkylation at the 3:2 ratio was 77.9 %, slightly lower than that of the 1:1 mass ratio at 79.2 % (Fig. 2f), proving that decreasing the proportion of Hβ is disadvantageous for the alkylation of NAP by the methyl species generated from CO_2 hydrogenation. Additionally, when the mass ratio of $ZnZrO_x$ to Hβ was 1:1, a handful of C1-C5 products were detected. This might be because the methoxy species generated on the $ZnZrO_x$ surface could not be promptly consumed by NAP adsorbed on Hβ over the $ZnZrO_x$/Hβ catalysts with mass ratio less than 1:1, indicating that the number of acidic sites was insufficient and there were no extra acidic sites to promote the C—C

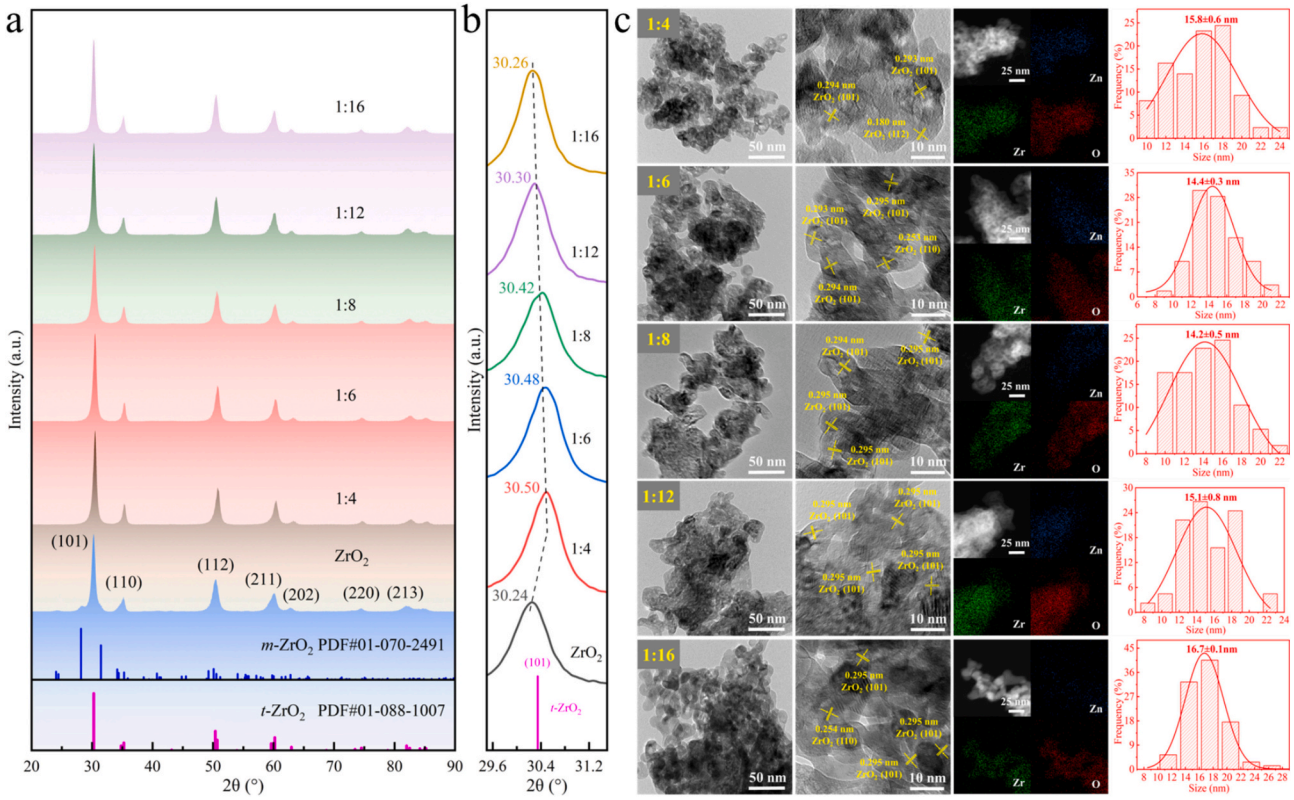

Fig. 3. Characterization results of $ZnZrO_x$ oxides with diverse Zn:Zr molar ratios. (a) XRD patterns at 2θ of 20–90°. (b) Magnifying view of 29.5–31.5°. (c) TEM, HRETM, HADDF-STEM elemental mapping images and particle size distribution histograms.

Table 1
Texture properties, oxygen vacancy concentration and H_2-D_2 exchange temperature of ZrO_2 and $ZnZrO_x$ samples.

Samples	$d_{(101)}$ (Å)	Specific surface area ($m^2 \cdot g^{-1}$)	Total pore volume ($cm^3 \cdot g^{-1}$)	Oxygen vacancy concentration (%)	Ignite H_2-D_2 exchange temperature (°C)
ZrO_2	2.953	37.4	0.2007	14.6	–
$Zn_1Zr_4O_x$	2.929	59.5	0.2976	21.9	129.4
$Zn_1Zr_6O_x$	2.930	46.8	0.2488	22.6	120.8
$Zn_1Zr_8O_x$	2.936	66.9	0.2671	24.8	112.6
$Zn_1Zr_{12}O_x$	2.947	45.5	0.2348	20.0	135.7
$Zn_1Zr_{16}O_x$	2.951	42.5	0.2250	18.5	142.5

coupling of methoxy substances diffused onto the zeolite to produce C1-C5. On the other hand, elevating the mass ratio leaded to a higher number of acidic sites, but a deficient of $ZnZrO_x$ sites failed to effectively convert CO_2 and H_2. Therefore, in both scenarios, only trace amounts of C1-C5 products were acquired, which were nearly undetectable. These phenomena were consistent with the conversion of CO_2 and NAP (Fig. 2e). At the mass ratio of 1:1, the CO_2 hydrogenation and NAP alkylation reactions reached an excellent match. The number of acidic sites was slightly in excess, enabling methoxy species diffused onto the zeolite to execute C—C coupling, thus yielding a small quantity of detectable C1-C5 products. Consequently, the $Zn_1Zr_8O_x$/Hβ catalyst with 1:1 mass ratio presented the uppermost coupling performance of 5.9 μmol·g-1 oxide·s^{-1}, showing the compatible synergy between hydrogenation and alkylation active sites and thereby affording superior catalytic efficiency.

3.1.4. Influence of intimacy of two active components on coupling performance

Since the spatial distribution of $ZnZrO_x$ and Hβ in the composite catalyst exerts momentous role in determining the coupling capacities, the impact of intimacy in $ZnZrO_x$/Hβ catalysts on the catalytic performances was studied. As shown in Fig. 2g, three preparation methods with varying intimacies were established: dual-bed (DB, cm-level intimacy), grinding-mixing (GM, μm-level intimacy), and co-precipitation (CR, nm-level intimacy). Evaluation results indicated that the assembly mode of DB exhibited the worst catalytic performances, with CO_2 and NAP conversions of only 17.7 % and 20.1 %, respectively (Fig. 2h), and a carbon usage for the alkylation pathway of just 72.9 % (Fig. 2i). The spatial distance between two active sites was relatively large, meaning that the reactive intermediates produced on $ZnZrO_x$ had to undergo a remote diffusion path before reaching the Hβ for the alkylation reaction. As a consequence, the effective synergistic action could not be achieved. Excitedly, the load strategy of GM intensified the conversions of CO_2 and NAP, showing alkylation selectivity of 79.2 %. This could be attributed to the shortened diffusion route resulting from strengthened intimacy between those active sites. In other words, elevating the intimacy between $ZnZrO_x$ and Hβ can accelerate the efficient reaction of CO_2 and NAP, thus intensifying the coupling reaction. Abnormally, the synthesis manner of CR owned the greatest intimacy delivered a slight decrease in conversion activities, but its coupling alkylation selectivity of 81.9 % was the uppermost among the three assembly strategies. This may be ascribed to the co-precipitation method, which caused $ZnZrO_x$ solid solution to deposit within the pores of Hβ, resulting in pore blockage that hindered reactant diffusion and consequently impaired catalytic activities. Nevertheless, co-precipitation enhanced the intimacy between active sites, leading to the strengthened alkylation selectivity. In addition, the influence of reaction temperature over these catalysts were also conducted, as exhibited in Fig. S6-S9. These phenomena points that improving the diffusivity in the $ZnZrO_x$/Hβ catalyst is desiderated for intensifying the coupling reaction.

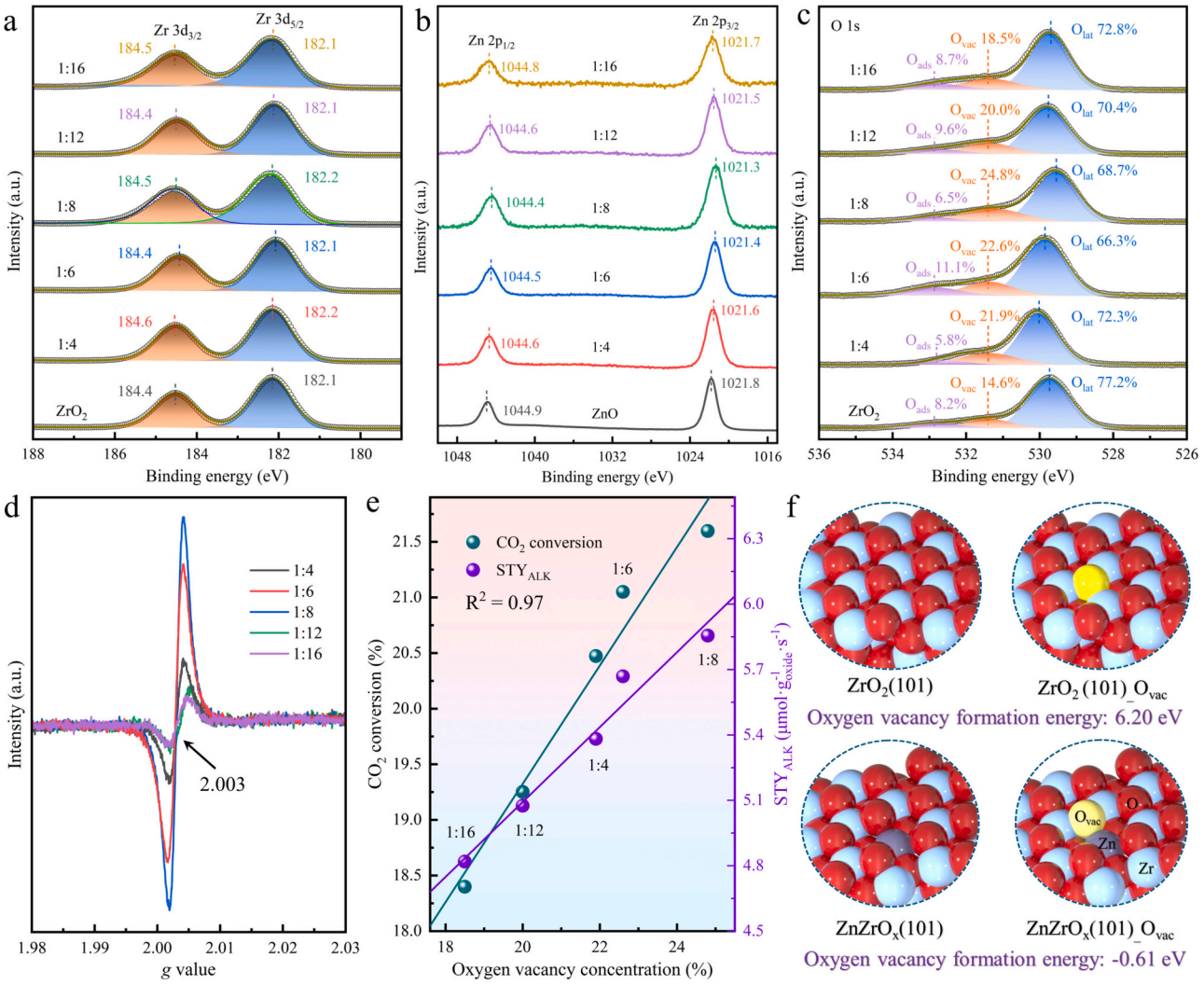

Fig. 4. Chemical properties of ZrO_2 and $ZnZrO_x$ samples. XPS spectra and peak fitting data of (a) Zr 3d, (b) Zn 2p and O 1 s. (d) EPR curves. (e) Linear relationship between CO_2 conversion and oxygen vacancy concentration in $ZnZrO_x$ solid solutions at 360 °C. (f) The oxygen vacancy formation energy of ZrO_2(101) and $ZnZrO_x$(101) surface.

3.1.5. Impact of GHSV on the conversion efficiency between hydrogenation and alkylation

Under optimized conditions, the influence of GHSV on the coupling reaction was disclosed over $Zn_1Zr_8O_x$/Hβ catalyst (Fig. 2j). At low GHSV of 3000 mL·g-1 cat·h^{-1}, the greatest catalytic activities were gained, whereas the selectivity of 76.7 % was the lowest for ANs compound. This decrease was ascribed to the longer residence time of intermediates, which promoted the sequential alkylation and cleavage reactions. With improving GHSV to 9000 mL·g-1 cat·h^{-1}, the conversions of CO_2 and NAP consecutively declined to 16.8 % and 25.9 %, respectively, while the selectivity to MMN reached the maximum of 70.2 %. Although lower GHSV favored higher reactant conversions, it also intensified undesirable cracking of NAP. In consequence, a GHSV of 6000 mL·g-1 cat·h^{-1} was identified as optimal, providing a balanced compromise between activity with ANs selectivity.

3.1.6. Stability evaluation of the coupling reaction over $Zn_1Zr_8O_x$/Hβ catalyst

The long-term stability of the $Zn_1Zr_8O_x$/Hβ catalyst prepared utilizing GM strategy was further performed, as depicted in Fig. 2k. Over a 100 h on stream, no significant deactivation was discovered in the conversions of CO_2 and NAP reactants. The CO_2 conversion remained stable at about 21.5 %, while the carbon usage involved in the alkylation pathway was maintained at approximately 80.3 %, demonstrating excellent catalytic stability and superb potential for industrial application.

3.2. Physicochemical characterization of as-synthesized $ZnZrO_x$/Hβ catalysts

3.2.1. Structural, textural and morphological natures of catalysts

To elucidate the performance discrepancies among the series $ZnZrO_x$/Hβ catalysts with varying Zn:Zr molar ratios, comprehensive characterizations were performed. The XRD patterns for $ZnZrO_x$ (Fig. 3a) displayed five apparent diagnostic peaks at 2θ of 30.2°, 35.2°, 50.5°, 60.1° and 62.9°, indexing to the (101), (110), (112), (211) and (202) crystal facets of tetragonal ZrO_2 (*t*-ZrO_2, PDF#01–088-1007) [43]. A tiny diffraction peak emerged at 28.3° in ZrO_2 sample ascribed to monoclinic ZrO_2 (*m*-ZrO_2, PDF#01–070-2491) [44], meaning the intergrowth of disparate ZrO_2 crystalline forms, with *t*-ZrO_2 being the predominant phase. This differs from the ZrO_2 oxide prepared employing ammonium carbonate as precipitant, which primarily shows *m*-ZrO_2 crystal phase [45]. In contrast, the topological architecture of *t*-ZrO_2 exhibits better catalytic activity in CO_2 hydrogenation [24,46], highlighting the superiority of oxalate-mediated precipitation method adopted in this work. Besides, the fingerprint of *m*-ZrO_2 phase

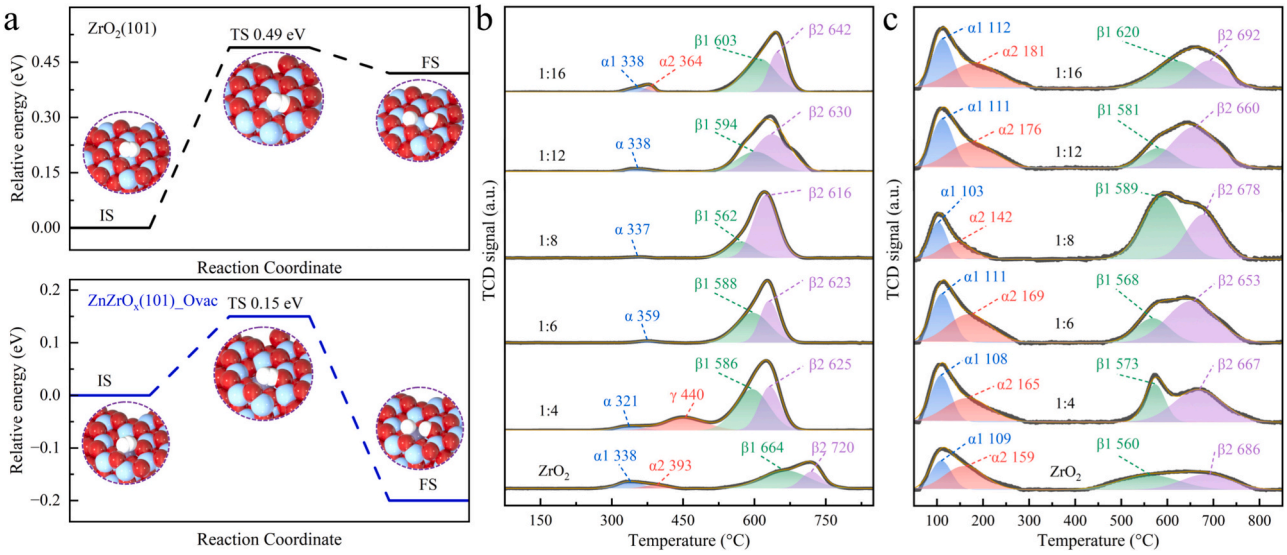

Fig. 5. (a) Relative energy for the dissociation of H_2 on ZrO_2(101) and $ZnZrO_x$(101)_O_v surface. (b) H_2-TPR and (c) CO_2-TPD curves of ZrO_2 and $ZnZrO_x$ samples with diverse Zn:Zr molar ratios.

disappeared in the prepared $ZnZrO_x$ after the introduction of Zn dopant, indicating the exclusive presence of the *t*-ZrO_2 phase. In Fig. 3b, it could be seen that the diffraction peaks shifted from 30.26° to 30.50° with elevating Zn doping amount, which can be ascribed to the substitutional incorporation of Zn^{2+} (0.74 Å) into *t*-ZrO_2 lattice replacing Zr^{4+} ions (0.82 Å) and thereby inducing a contraction of the crystal unit cell [47]. This observation is consistent with the lattice spacing variation trend of the (101) plane calculated using Scherrer equation (Table 1). No apparent characteristic peaks of ZnO were monitored (PDF#01-070-8070) [48], indicating the uniform dispersion of Zn throughout the $ZnZrO_x$ and confirming the formation of solid solution construction. That is, there were abundant asymmetric Zn-O-Zr sites in the $ZnZrO_x$ solid solution. In addition, the crystallinity of $ZnZrO_x$ sample synthesized via oxalate-mediated precipitation tactics was memorably lower than that prepared using ammonium carbonate as precipitant, suggesting the presence of more crystal defects, possibly oxygen vacancies (Fig. S10). Therefore, enhanced coupling performances were obtained. Attentively, XRD and thermogravimetric (TG) measurements were also conducted on the $Zn_1Zr_8O_x$/Hβ catalyst before and after stability evaluation. As shown in Fig. S11a, both the spent and fresh $Zn_1Zr_8O_x$/Hβ catalysts exhibited characteristic diffraction peaks of Hβ zeolite at 7.6°, along with $ZnZrO_x$ at 30.4°, indicating that the crystalline architectures of the composite catalyst remained intact after the long-term reaction. In addition, two vulnerable fingerprints appeared at 42.6° and 55.3° in the spent catalyst, which might be attributed to minor residues of liquid products on the surface. Furthermore, TG analysis (Fig. S11b) disclosed that the spent $Zn_1Zr_8O_x$/Hβ catalyst had only a 6.6 % weight loss, suggesting excellent resistance to carbon deposition. Therefore, $Zn_1Zr_8O_x$/Hβ catalyst demonstrated ascendant catalytic stability in the coupling reaction.

The textural properties of $ZnZrO_x$ solid solutions were analyzed using N_2 adsorption-desorption isotherms. As displayed in Fig. S12, all the samples illustrated representative IV isotherm with H3 hysteresis loop emerging around $P/P_0 = 0.45$, meaning the mesoporous structure [49]. Moreover, it was noticed that those solid solutions with different Zn:Zr ratios delivered various surface areas and pore volume (Table 1), indicating that the textural properties could be tuned by means of adjusting the Zn doping level. Notably, the supreme specific surface area of 66.9 $m^2 \cdot g^{-1}$ was acquired on the $Zn_1Zr_8O_x$ sample, implying a more developed porous architectures achieved with an optimal accession quantity of Zn incorporation. Such porous structure is profitable for increasing the accessible surface area and exposing a greater number of active sites, which is consistent with the outcome of catalytic evaluation (Fig. 2a). Additionally, the textural characteristics of the catalysts synthesized via the three different preparation methods (Fig. 2g) were also investigated. In Fig. S13 and Table S1, the $Zn_1Zr_8O_x$/Hβ (CR) provided a surface area of 235.8 $m^2 \cdot g^{-1}$, which was 28.9 $m^2 \cdot g^{-1}$ lower that of $Zn_1Zr_8O_x$/Hβ (GM). Its pore volume also decreased from 0.2584 $cm^3 \cdot g^{-1}$ to 0.2114 $cm^3 \cdot g^{-1}$, indicating that the CR strategy led to the partial deposition of oxide within the pores of Hβ zeolite. This pore blockage is inferred to contribute to the deteriorated catalytic activity obtained on the CR catalyst (Fig. 2h).

Fig. 3c shows the morphologies, elemental mapping and particle size distributions of $ZnZrO_x$ solid solutions. Irregular ellipsoidal appearances were discovered in the TEM images, a representative feature commonly associated with the materials prepared via precipitation method [50]. Notably, the Zn dosage concentration evidently affected the particle dispersion, displaying an initial improvement followed by a decline as the Zn:Zr ratios changed from 1:4 to 1:16. Among them, the $Zn_1Zr_8O_x$ sample showed the optimal dispersion with the smallest average size of 14.16 nm. HRTEM images revealed interplanar spacings of 0.293–0.295 nm, corresponding to the *t*-ZrO_2 (101) facets, in agreement with the XRD data. In particular, $ZnZrO_x$/Hβ catalysts with greater Zn doping content depicted contractible lattice fringes (Fig. 3b). Elemental mapping further corroborated the uniform distribution of Zn in $ZnZrO_x$ and the generation of solid solution structure, signifying strong interactions between Zn and Zr species. However, in the $Zn_1Zr_4O_x$ sample, localized regions with relatively high Zn content were noticed, suggesting the presence of small quantities of ZnO particles. This observation explained why excessive Zn in $ZnZrO_x$/Hβ could be detrimental to the coupling properties (Fig. 2a). Furthermore, numerous darker contrast regions were identified in the HAADF-STEM images of $ZnZrO_×$, indirectly manifesting the existence of structural defects within the solid solutions. The abundance of these dark contrast regions consolidated with Zn:Zr ratios from 1:4 to 1:8. Nevertheless, upon further raising the ratio to 1:16, a uniform and symmetrical contrast distribution emerged, implying that $Zn_1Zr_8O_x$ had a comparatively higher concentration of defects. More imperfection frameworks are beneficial for the generation of coordinatively unsaturated active sites, strengthening CO_2 adsorption and activation [51–53]. These findings align well with the activity evaluations in Fig. 2, wherein $Zn_1Zr_8O_x$/Hβ showed the superior hydrogenation coupling performances.

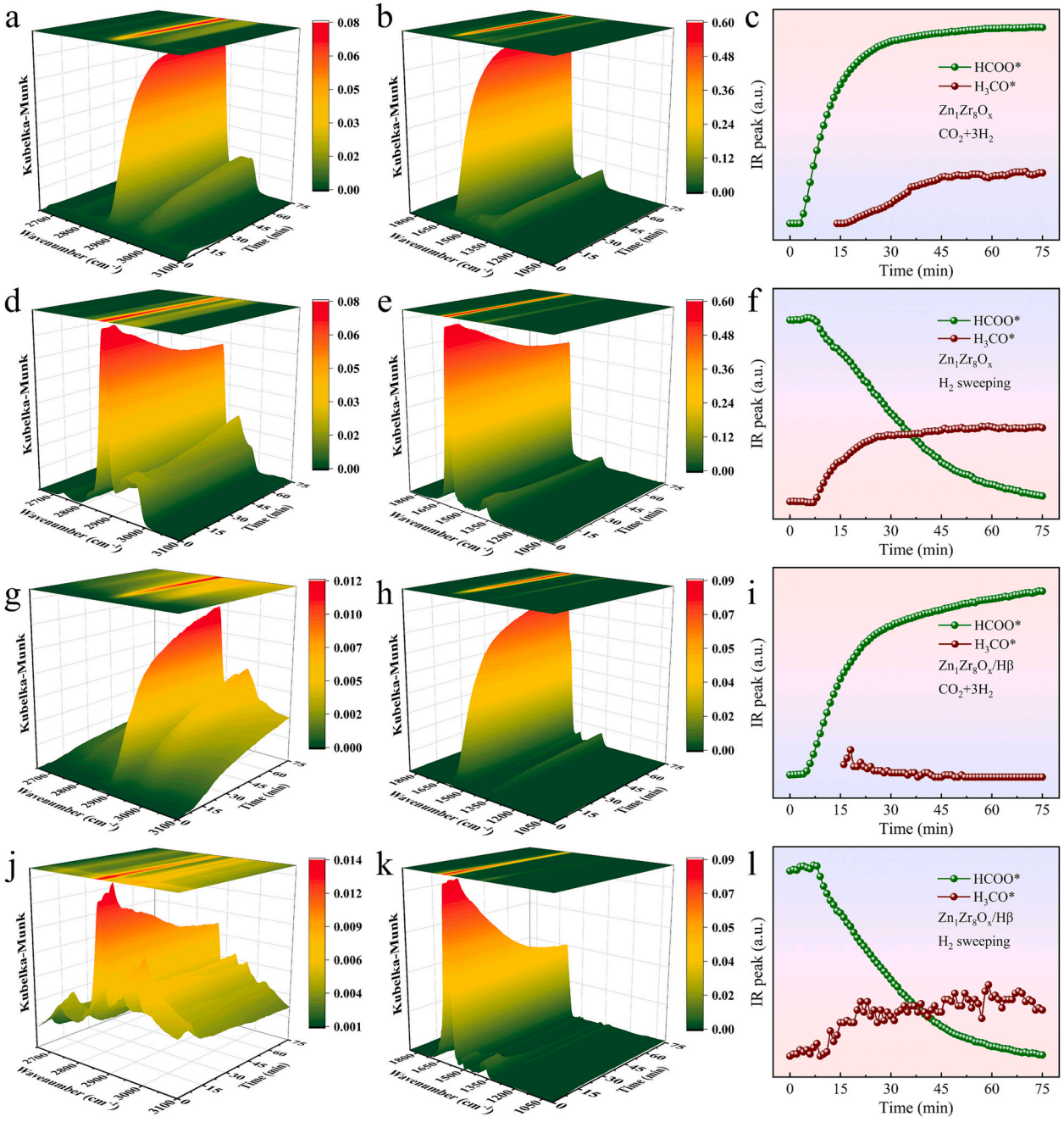

Fig. 6. In situ DRIFTS investigation of CO_2 hydrogenation. (a, b, c) Spectra and the variation of intermediate species concentration over $Zn_1Zr_8O_x$ under the atmosphere of $CO_2 + 3H_2$. (d, e, f) Spectra and the variation of intermediate species concentration over $Zn_1Zr_8O_x$ after switching to H_2 atmosphere. (g, h, i) Spectra and the variation of intermediate species concentration over $Zn_1Zr_8O_x$/Hβ under the atmosphere of $CO_2 + 3H_2$. (j, k, l) Spectra and the variation of intermediate species concentration over $Zn_1Zr_8O_x$/Hβ after switching to H_2 atmosphere.

3.2.2. *Electronic interactions and chemical properties of catalysts*

For the sake of expounding the electronic interactions among Zn, Zr and O species in the $ZnZrO_x$ solid solutions, XPS tests were executed and compiled in Fig. 4. Two distinct peaks assigned to Zr $3d_{5/2}$ and Zr $3d_{3/2}$ orbits were observed at 182.1 eV and 184.4 eV, respectively (Fig. 4a,), suggesting the predominant valence state of Zr^{4+} in pure ZrO_2 and $ZnZrO_x$ samples [41,54,55]. Compared with ZrO_2, the Zr 3d spectra of $ZnZrO_x$ displayed a slight excursion toward higher binding energies, indicating electron withdrawal from Zr species due to interactions. Furthermore, variations in Zn:Zr ratios within the $ZnZrO_x$ solid solutions prominently influenced the binding energies of Zn 2p orbits (Fig. 4b). Specially, sole ZnO demonstrated Zn $2p_{3/2}$ and Zn $2p_{1/2}$ binding energies at 1021.8 eV and 1044.9 eV, respectively [56]. For $Zn_1Zr_4O_x$ sample, the Zn 2p binding energy shifted negatively by about 0.2 eV from 1021.8 eV to 1021.6 eV. Upon further elevating Zn:Zr molar ratio to 1:8, the binding energy of Zn 2p declined to 1021.3 eV, and subsequently exhibited a slight rebound at lower Zn doping contents. This tendency expressly demonstrated electron perturbation between Zn and Zr species, resulting in electron-rich Zn and electron-deficient Zr sites. Attentionally, electron-rich Zn species have stronger capability for H_2 dissociation [57], which was conducive to boosting CO_2 hydrogenation performances. Interestingly, $Zn_1Zr_4O_x$ and $Zn_1Zr_6O_x$ with greater Zn content depicted weaker electron transfer effect than $Zn_1Zr_8O_x$ sample. This could be attributed to the excessive Zn impairing its effective distribution in ZrO_2 crystal lattices, resulting in the formation of isolated ZnO and consequently weakening the interactions. Hence, the electronic

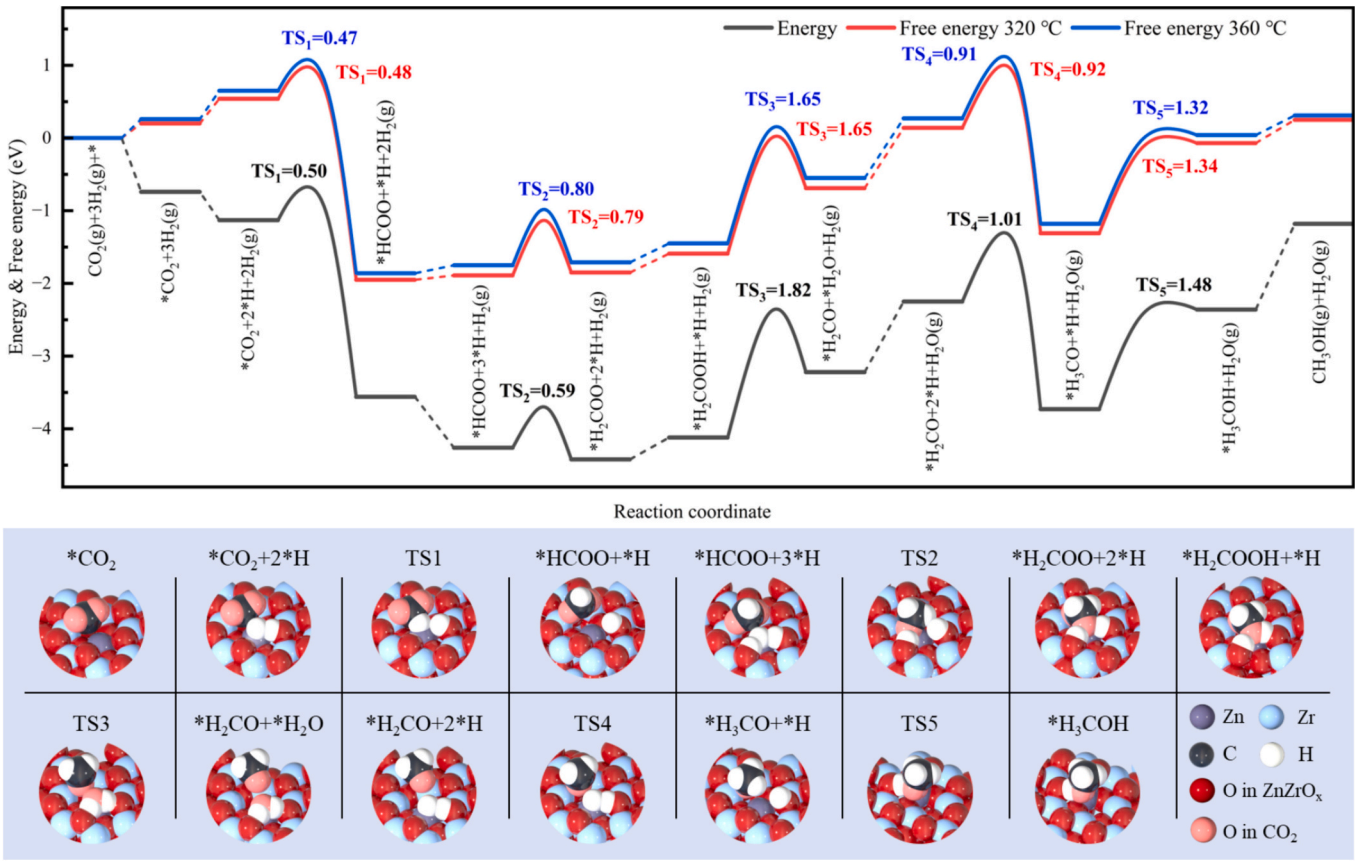

Fig. 7. Energy and free energy calculated at 320 and 360 °C under 4 MPa for the hydrogenation of CO_2 to CH_3OH on $ZnZrO_x(101)\_O_v$ surface.

perturbation in $ZnZrO_x$ solid solutions can be effectively regulated by tuning the Zn incorporation level. Due to the valence mismatching between Zn^{2+} and Zr^{4+} cations, the doping of Zn into ZrO_2 lattice is usually accompanied by the generation of oxygen vacancy, which is responsible for the adsorption and excitation of CO_2. After deconvolution, three characteristic orbits in Fig. 4c were distinguished at around 529.6 eV, 531.4 eV and 532.9 eV, attributing to the lattice oxygen (O_{lat}), oxygen vacancies (O_{vac}) and weakly adsorbed oxygen species and/or surface hydroxyl groups (O_{ads}), respectively [52,58]. The fabricated $ZnZrO_x$ samples demonstrated greater O_{vac} content than sole ZrO_2 (14.6 %) and the evolution of O_{vac} in the series $ZnZrO_x$ with diverse Zn:Zr ratios was in line with the variation of Zn 2p binding energies (Fig. 2b). Of which the maximum O_{vac} of 24.8 % was achieved in $Zn_1Zr_8O_x$ solid solution. According to the results of TEM and BET, the $Zn_1Zr_8O_x$ had the smallest particle size of 14.2 nm and maximal specific surface area of 66.9 $m^2 \cdot g^{-1}$ (Fig. 3c and Table 1). It could be deduced that the O_{vac} level is compactly concerned to the dispersion and exposed surface area of $ZnZrO_x$. In addition, these phenomena also proved that the electronic interactions and O_{vac} density within $ZnZrO_x$ solid solutions can be availably regulated by tuning the Zn:Zr molar ratio, which in turn affected the catalytic properties of $ZnZrO_x$/Hβ catalysts in coupling CO_2 hydrogenation with NAP alkylation. Consistently, as illustrated in Fig. S14, the O_{vac} content of $ZnZrO_x$(AC) was 14.5 %, which was lower than that of $ZnZrO_x$(OA) at 21.9 %, indicating that the importance of oxygen vacancy in strengthening the coupled transformation activities.

The concentrations of O_{vac} in prepared $ZnZrO_x$ solid solutions were further identified using EPR. As demonstrated in Fig. 4d. distinct resonance peak located at *g* value of 2.003 was assigned to the acquisition of unpaired electrons on O_{vac} sites [59]. Besides, the intensity of EPR signal reduced in the order of 1:8 > 1:6 > 1:4 > 1:12 > 1:16, confirming the most abundant O_{vac} in the $ZnZrO_x$ sample with Zn:Zr ratio of 1:8. This was in line with the O 1 s spectra (Fig. 4c). In order to better understand the differences in coupling activities induced by the variation of Zn:Zr ratios in $ZnZrO_x$/Hβ catalysts, the conversion of CO_2 and STY_{ALK} at 360 °C were correlated with the concentration of oxygen vacancy (Fig. 4e). The catalytic performances steadily strengthened with raising O_{vac} level and a satisfying linear relationship was obtained. Improving O_{vac} amount can boost the conversion of CO_2, generating luxuriant active intermediates for alkylation and leading to the efficient coupling progress. In addition, $ZrO_2(101)$ and $ZnZrO_x(101)$ surfaces were modeled to study the formation energy of O_{vac} (Fig. 4f). For $ZrO_2(101)$, the O_{vac} formation energy was 6.20 eV, which was relatively high, manifesting that a higher reduction temperature was required to facilitate the generation of O_{vac}. In contrast, $ZnZrO_x(101)$ exhibited a formation energy of −0.61 eV, implying that O_{vac} were spontaneously yielded after the introduction of Zn into the ZrO_2 lattice. Therefore, it can be deduced that an appropriate incorporation level of Zn will reinforce the electronic interaction in $ZnZrO_x$ and promote the formation of abundant oxygen defects. When excessive Zn species is doped, it may result in the production of ZnO particles, hindering the catalytic performance of $ZnZrO_x$ solid solutions.

Fig. 5a depicts the dissociation of H_2 on the surfaces of ZrO_2 and $ZnZrO_x(101)\_O_{vac}$ slabs. It could be seen that H_2 molecules tend to adsorb in a planar configuration on the oxide surface and then undergo heterogeneous dissociation. The dissociation energy barrier of H_2 on the ZrO_2 (101) was 0.49 eV, which was 0.34 eV taller than the 0.15 eV obtained on $ZnZrO_x(101)\_O_{vac}$ surface. This indicated that the introduction of Zn significantly intenified H_2 activation capability, which was further vertified through H_2-D_2 exchange measurements. With increasing Zn:Zr molar ratio from 1:4 to 1:16, the ignite temperature for H_2-D_2 exchange first declined and then improved (Table 1). Concurrently, the lowest exchange temperature of 112.6 °C was gained on the $Zn_1Zr_8O_x$ solid solution ascribed to its superior dispersion of Zn and strong electronic interactions, confirming the superior dispersion.

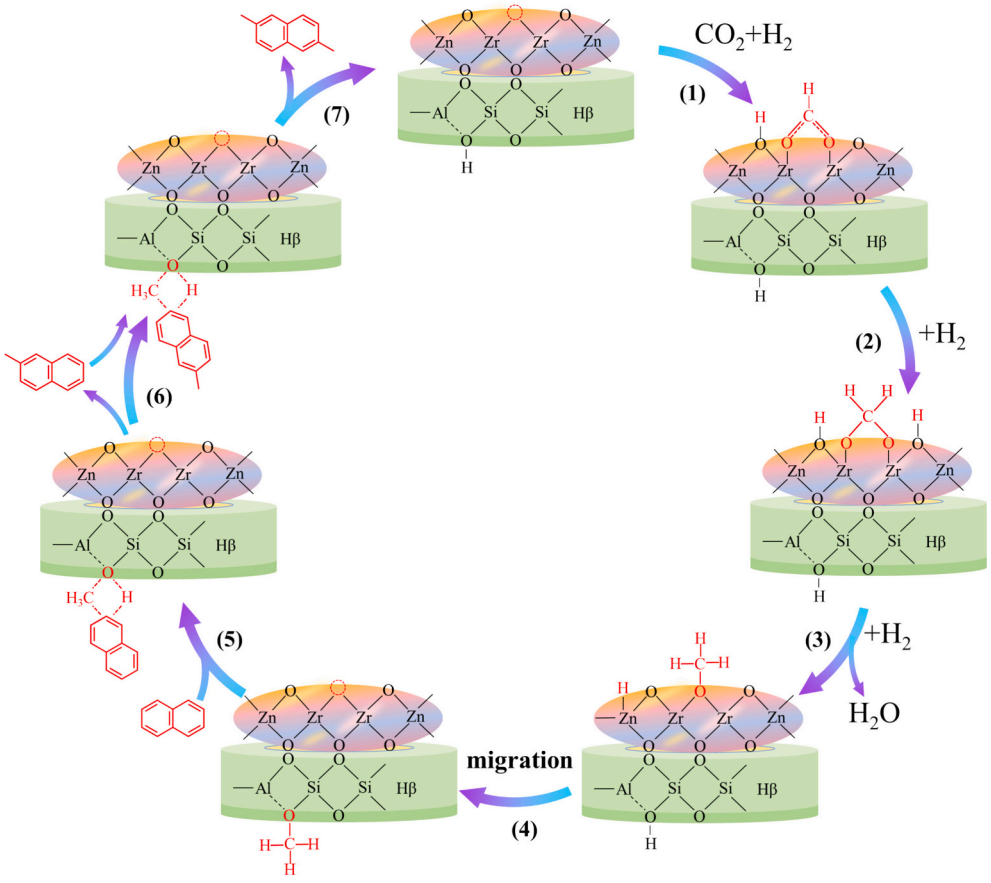

Fig. 8. Proposed reaction mechanism of CO_2 hydrogenation coupling with naphthalene alkylation over $ZnZrO_x$/Hβ catalyst.

Moreover, the reducibility and mutual impacts of Zn and Zr in $ZnZrO_x$ solid solutions were characterized by utilizing H_2-TPR and the profiles are provided in Fig. 5b. For pure ZrO_2 sample, the H_2 consumption peaks centered around 360 °C (α) were assigned to the reduction of surface-adsorbed oxygen species, while those peaks at 664 °C (β1) and 720 °C (β2) corresponded to the reduction of surface and bulk lattice oxygen in ZrO_2, respectively [34,38]. Interestingly, the synthesized $ZnZrO_x$ solid solutions displayed semblable reduction characteristics, but the peak β shifted observably toward lower temperature. This manifested the generation of asymmetric Zn-O-Zr sites, which were more readily reduced and thereby promoting the bulk ZrO_2 reduction [24]. Moreover, a distinct peak (γ) was observed at 440 °C for the $ZnZrO_x$ with ratio of 1:4, corresponding to the reduction of isolated Zn species [60], This confirmed that excessive incorporation of Zn resulted in the uneven dispersion, which impaired the electronic interactions between Zn and Zr species. Prominently, the $Zn_1Zr_8O_x$ solid solution presented the lowest reduction temperature, illustrating that oxygen vacancies were more readily formed. This agrees well with the results from XPS and EPR analyses (Fig. 4). Furthermore, the CO_2 adsorption capacity of $ZnZrO_x$ solid solutions were characterized by CO_2-TPD as depicted in Fig. 5c. It could be observed that two apparent desorption peaks arisen at low temperature (α) of 100 °C and high temperature (β) of 650 °C, which were attributed to the desorption of physically adsorbed CO_2 and chemisorbed CO_2 in oxygen vacancies, respectively [34,57]. Obviously, the $Zn_1Zr_8O_x$ solid solution delivered the most desorption amount of CO_2 due to the abundant oxygen vacancies than the other $ZnZrO_x$ samples with varying Zn:Zr molar ratios.

3.3. Mechanistic investigation on the pathways of CO_2 hydrogenation coupling with naphthalene alkylation

In situ DRIFTS spectra were executed to explore the coupling mechanism of CO_2 hydrogenation and NAP alkylation. A gas mixture of $CO_2 + 3H_2$ was introduced over either the single $Zn_1Zr_8O_x$ solid solution or the composite $Zn_1Zr_8O_x$/Hβ catalyst, and the associative spectra collected at 320 °C under 0.2 MPa are provided in Fig. 6. On the individual $Zn_1Zr_8O_x$, characteristic bands at 2975 cm^{-1} and 2876 cm^{-1} (Fig. 6a) were found attributing to the C—H vibration in bidentate *HCOO species, while spectral bands located at 1588 cm^{-1} and 1372 cm^{-1} (Fig. 6b) were assigned to the asymmetric and symmetric O-C-O stretching vibrations [42,61]. Besides, faint peaks at 1506 cm^{-1} and 1305 cm^{-1} were ascribed to bCO2–3 and bHCO- 3 substances, respectively [62]. Table S2 summarized the intermediates of CO_2 hydrogenation and corresponding peak assignments. The Kubelka-Munk intensity of *HCOO bands gradually improved with prolonged reaction time, manifesting that CO_2 was motivated on the surface of $Zn_1Zr_8O_x$ and transformed into *HCOO intermediates. In the meantime, diagnostic bands associated with *H_3CO species were identified at 2929 cm^{-1}, 2820 cm^{-1} and 1456 cm^{-1}, corresponding to the C—H vibrations, along with bands situated at 1052 cm^{-1} and 1026 cm^{-1} belonging to the C—O stretching vibrations [63]. These distinct features turned into increasingly pronounced with prolonged exposure to the $CO_2 + 3H_2$ gas and attained an impassive state after approximately 45 min (Fig. 6c). Subsequently, the gas mixture was replaced with pure H_2 to probe the hydrogenation stage. Overtly, a continuous decline in the vibrational intensity of *HCOO species was presented, while the typical bands of H_3CO* species heightened correspondingly (Fig. 6d-f), demonstrating that *HCOO was further hydrogenated to form *H_3CO. These results confirm that CO_2 was converted into *H_3CO via the formate route over

a

Fuels	Doping content (wt%)	Density ($g \cdot mL^{-1}$)	Viscosity ($mm^2 \cdot s^{-1}$)	ID (ms)
HA-1	10	0.942	2.89	2548
HA-2	20	0.949	2.76	2276
JP-10	-	0.936	3.10	2752

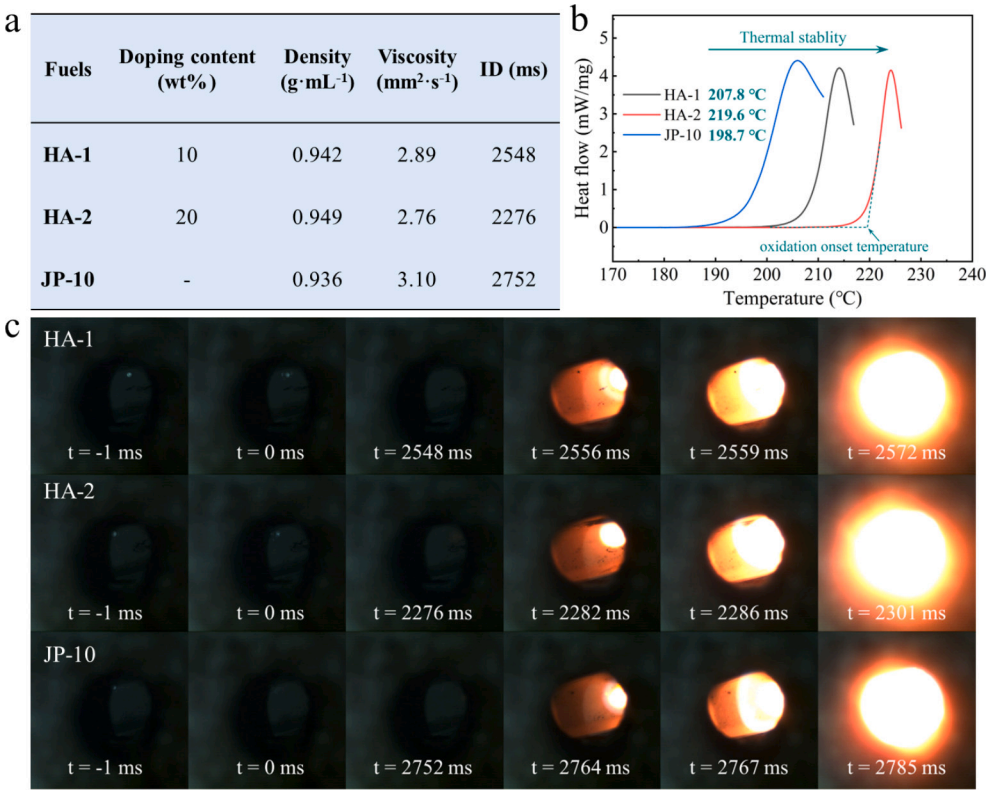

Fig. 9. Fuel properties of as-synthesized fuel components blended with JP-10. (a) Basic physicochemical property data. (b) Oxidation onset temperature measured by PDSC. (c) Photographs of fuel combustion flame.

the standalone $Zn_1Zr_8O_x$ sample [25,64]. For composite $Zn_1Zr_8O_x$/Hβ catalyst, the characteristic fingerprints of bidentate *HCOO and $*H_3CO$ substances were also detected (Fig. 6g-h). Nevertheless, the intensity of these tagged bands was lower than those obtained on the single $Zn_1Zr_8O_x$, and a longer stabilization time was required to accomplish the steady state (Fig. 6i). This behavior could be attributed to the migration of active intermediates from the active sites in solid solution to the Hβ zeolite, where the $*H_3CO$ species were subsequently consumed at the acidic sites. Visibly, a more rapid decline in *HCOO intensity during the hydrogenation stage was discovered on the $Zn_1Zr_8O_x$/Hβ catalyst, accompanied by a fluctuating enhancement in $*H_3CO$ signals (Fig. 6j-l). It verifies that CO_2 molecule was converted to $*H_3CO$ species on the surface of $Zn_1Zr_8O_x$, rather than generating CH_3OH and diffusing to the Hβ zeolite for the Friedel-Crafts alkylation. Additionally, this mechanistic insight explains the superior selectivity toward ANs found in the CO_2 hydrogenation coupling with NAP alkylation, because direct alkylation of NAP with CH_3OH usually requires higher reaction temperature, which frequently bring about severe side reactions [23,40,65].

The DFT calculations were further conducted to investigate the detailed reaction mechanisms of CO_2 hydrogenation. According to XRD and TEM analysis data (Fig. 3), the $ZnZrO_x$ solid solution predominantly exposed the (101) plane, which was thereby chosen for simulating the hydrogenation process. Fig. 7 depicts the geometrically optimized configurations and reaction energy diagrams for the production of CH_3OH from CO_2 hydrogenation on $ZnZrO_x$(101) surface. Initially, the possible adsorption sites of CO_2 were investigated, and it was discovered that CO_2 tends to adsorb in bidentate configuration at the oxygen vacancy of $ZnZrO_x$(101) slab, interacting with two adjacent Zr atoms [52,66]. The adsorption energy of CO_2 on $ZnZrO_x$(101) was calculated to be −0.74 eV, implying strong chemisorption. Moreover, the formation of *HCOO intermediate exhibited a reaction energy of −2.43 eV and an energy barrier (TS1) of 0.50 eV, suggesting that the transformation of CO_2 to *HCOO was thermodynamically and kinetically profitable. Next, the *HCOO was required to surmount an energy barrier of 0.59 eV (TS2) to form *HCOOH substance. The subsequent hydrogenation of *HCOOH led to the generation of $*H_2COOH$ species, with a reaction energy of 0.30 eV, indicating that this step is thermodynamically unfavorable. Thereafter, the terminal -OH group of $*H_2COOH$ reacted with *H and underwent C—O cleavage to produce $*H_2CO$ and $*H_2O$ species, exhibiting the maximum energy barrier of 1.82 eV (TS3) among all the elementary steps. This step is identified as the rate-determining step for the hydrogenation of CO_2 to CH_3OH over the $ZnZrO_x$ solid solution. Ultimately, the $*H_2CO$ was further hydrogenated into $*H_3CO$ species (TS4 = 1.01 eV), and the $*H_3COH$ was yielded by the hydrogenation of $*H_3CO$ species. In addition, Gibbs free energy corrections were applied to reflect more realistic reaction conditions. Consequently, the free energy profiles under conditions of 320 °C and 360 °C under 4 MPa were obtained. It was distinctly found that the energy of *HCOO and $*H_3CO$ species were at local minima, demonstrating that these two substances are crucial active intermediates and relatively stable, which is consistent with the in situ DRIFTS observations.

On the strength of the above experimental and computational results, a catalytic mechanism was proposed for the directional synthesis of high-density aviation fuels via CO_2 hydrogenation coupling with NAP alkylation. As shown in Fig. 8, H_2 molecule is stimulated at the Zn—O site and undergoes heterolytic dissociation to produce hydrogen species, which then react with CO_2 adsorbed in bidentate configuration at the oxygen vacancies to form *HCOO (1). This intermediate is further hydrogenated into $*H_2COO$ (2). Subsequently, $*H_3CO$ is yielded by sequential hydrogenation and dehydration steps (3). Next, $*H_3CO$ species migrate to the acidic sites of Hβ zeolite (4), where it conducts Friedel-Crafts alkylation with NAP (5), contributing to the generation of MMN (6). Furthermore, the acquired MMN can also proceed continuous alkylation at the acidic sites to yield polyalkyl substituted NAP (7). The asymmetric Zn-O-Zr sites and oxygen vacancies are momentous active sites in the coupling reaction. Superior dispersion of Zn illustrates

stronger electronic interactions with Zr species, which intensifies the excitation of CO_2 and H_2, resulting in the yield of abundant $*H_3CO$ intermediate that subsequently participate in the alkylation reaction of NAP.

3.4. The fuel properties of as-synthesized high-density aviation fuel

The synthesized ANs substances can be employed as components of high-density aviation fuel, and the impact on fuel properties was assessed by evaluating their performance as additives to JP-10, a widely utilized high-density aviation fuel initially developed for the U.S. Tomahawk cruise missile, featured by a density of 0.936 $g{\cdot}mL^{-1}$ and a kinematic viscosity of 3.10 $mm^2{\cdot}s^{-1}$ [67]. From Fig. 9a, with the increase in doping content, the fuel density increased significantly, and the viscosity was also notably reduced. At a high blending level of 20 wt%, the density of HA-2 fuel risen to 0.949 $g{\cdot}mL^{-1}$, while the viscosity decreased to 2.76 $mm^2{\cdot}s^{-1}$, illustrating that the ANs possessed superior properties for the application in high-density aviation fuel. Besides, the addition of ANs dramatically promoted thermal stability, as evidenced by higher oxidation onset temperature (Fig. 9b). This improvement is advantageous for maintaining fuel integrity, particularly under high-speed flight where the fuel tank experiences rapid temperature increases because of aerodynamic heating from air friction [68,69]. In Fig. 9c, HA fuels with the use of ANs also presented shortened ignition delay time (ID) in contrast with JP-10 (2752 ms). The ID of 2548 ms and 2276 ms were gained for HA-1 and HA-2, respectively. This can accelerate the rapid release of energy from the employed high-density aviation fuel, thereby promoting supersonic flight capabilities of aircraft.

4. Conclusions

In this work, series $ZnZrO_x$/Hβ catalysts were synthesized using oxalate-mediated precipitation method, aiming to achieve the directional synthesis of high-density aviation fuel on the basis of CO_2 hydrogenation coupling naphthalene alkylation. The electronic interactions in $ZnZrO_x$ solid solutions could be regulated by adjusting the Zn doping concentration. Comprehensive characterization results illustrated that the electron perturbation from Zr to Zn effectively enhanced the hydrogen dissociation capacity and the generation of oxygen vacancy, which further improved the adsorption and activation of CO_2 and facilitated the production of $*H_3CO$ species that subsequently diffused into Hβ zeolite for the alkylation of NAP. Specially, the $Zn_1Zr_8O_x$/Hβ catalyst exhibited the optimum coupling selectivity of 86.4 % and STY_{ALK} of 5.9 μmol·g-1 oxide·s^{-1} toward ANs with conversions of 21.6 % for CO_2 and 28.4 % for NAP at 360 °C, and excellent catalytic stability was also observed. Additionally, in situ and DFT simulations further verified that the generation of $*H_3CO$ on $ZnZrO_x$, which was then transferred to the pores of Hβ zeolite to participate alkylation. Finally, a transformation pathway for the preparation of ANs was proposed. After blending with JP-10 fuel, strengthened density of 0.949 $g{\cdot}mL^{-1}$, improved oxidation onset temperature of 219.6 °C and shortened ignition delay time of 2276 ms were acquired, implying the superior fuel property synthesized by coupling CO_2 hydrogenation with NAP alkylation and excellent application prospects in high-density aviation fuels.

CRediT authorship contribution statement

Xiaopo Niu: Validation, Methodology, Investigation, Funding acquisition, Formal analysis, Data curation. **Hongming Qian:** Visualization, Investigation, Formal analysis, Data curation. **Dongyuan Cai:** Investigation, Formal analysis. **Wenli Zhao:** Investigation, Data curation. **Qingfa Wang:** Resources, Investigation. **Quanli Ke:** Formal analysis, Data curation. **Guokai Cui:** Investigation, Funding acquisition. **Chunliang Ge:** Methodology, Investigation. **Lina Tang:** Resources, Project administration. **Hanfeng Lu:** Resources, Project administration, Funding acquisition.

Declaration of competing interest

The authors declare that they have no known competing financial interests or personal relationships that could have appeared to influence the work reported in this paper.

Acknowledgments

The financial supports from the Key Research and Development Projects of Zhejiang Province (2024C03108, 2024C03114), the China Postdoctoral Science Foundation (2024M752867) and the Basic Public Welfare Research Program of Zhejiang Province (LTGS24E080008) are gratefully acknowledged. The authors also thank the team at Shiyanjia Lab (www.shiyanjia.com) for assistance with material characterization.

Appendix A. Supplementary data

Supplementary data to this article can be found online at https://doi.org/10.1016/j.cej.2025.166241.

Data availability

Data will be made available on request.

References

[1] Z. Shen, C. Liu, T. Wang, C. Shi, L. Pan, Z. Huang, X. Zhang, J.-J. Zou, Aqueous hydroalkylation of phenols for synthesis of high-density bicyclic alkane fuels, Chem. Eng. Sci. 305 (2025) 121176.
[2] J.-J. Zou, X. Zhang, L. Pan, High-Energy-Density Fuels for Advanced Propulsion: Design and Synthesis, John Wiley & Sons, Weinheim, 2020.
[3] L. Wang, F. Han, G. Li, M. Zheng, A. Wang, X. Wang, T. Zhang, Y. Cong, N. Li, Direct synthesis of a high-density aviation fuel using a polycarbonate, Green Chem. 23 (2021) 912–919.
[4] C. Bergero, G. Gosnell, D. Gielen, S. Kang, M. Bazilian, S.J. Davis, Pathways to net-zero emissions from aviation, Nature Sustainability 6 (2023) 404–414.
[5] V. Undavalli, O.B. Gbadamosi Olatunde, R. Boylu, C. Wei, J. Haeker, J. Hamilton, B. Khandelwal, Recent advancements in sustainable aviation fuels, Prog. Aerosp. Sci. 136 (2023) 100876.
[6] F. Lu, L. Li, Y. Yu, G. Tian, H. Xiong, J. Miao, F. Wei, C. Zhang, Road to carbon-neutral aviation: one-step conversion of CO_2 to sustainable aviation fuels, Ind. Eng. Chem. Res. 64 (2025) 3118–3135.
[7] E.V. Ramos-Fernandez, J.L. Santos, D.K. Alsaadi, A. Bavykina, J.M.R. Gallo, J. Gascon, Potential pathways for CO_2 utilization in sustainable aviation fuel synthesis, Chem. Sci. 16 (2025) 530–551.
[8] C. Hepburn, E. Adlen, J. Beddington, E.A. Carter, S. Fuss, N. Mac Dowell, J.C. Minx, P. Smith, C.K. Williams, The technological and economic prospects for CO_2 utilization and removal, Nature 575 (2019) 87–97.
[9] B. Yao, T. Xiao, O.A. Makgae, X. Jie, S. Gonzalez-Cortes, S. Guan, A.I. Kirkland, J. R. Dilworth, H.A. Al-Megren, S.M. Alshihri, P.J. Dobson, G.P. Owen, J.M. Thomas, P.P. Edwards, Transforming carbon dioxide into jet fuel using an organic combustion-synthesized Fe-Mn-K catalyst, Nat. Commun. 11 (2020) 6395.
[10] J. Ye, N. Dimitratos, L.M. Rossi, N. Thonemann, A.M. Beale, R. Wojcieszak, Hydrogenation of CO_2 for sustainable fuel and chemical production, Science 387 (2025) eadn9388.
[11] S. Ahmed, M.K. Khan, J. Kim, Revolutionary advancements in carbon dioxide valorization via metal-organic framework-based strategies, Carbon Capture Science & Technology 15 (2025) 100405.
[12] S. Ahmed, M.S. Hussain, M.K. Khan, J. Kim, Innovations in catalysis towards efficient electrochemical reduction of CO_2 to C_1 chemicals, J. Energy Chem. 107 (2025) 622–649.
[13] M.K. Khan, S. Ahmed, S.S. Bibi, A. Helaley, X. Liang, J. Kim, Advances in CO_2 hydrogenation: mechanisms and catalysts for alcohol synthesis, Chem. Eng. J. 517 (2025) 164209.
[14] M.T. Arslan, G. Tian, B. Ali, C. Zhang, H. Xiong, Z. Li, L. Luo, X. Chen, F. Wei, Highly selective conversion of CO_2 or CO into precursors for kerosene-based aviation fuel via an aldol–aromatic mechanism, ACS Catal. 12 (2022) 2023–2033.
[15] X. Wang, T. Jia, L. Pan, Q. Liu, Y. Fang, J.-J. Zou, X. Zhang, Review on the relationship between liquid aerospace fuel composition and their physicochemical properties, Transactions of Tianjin University 27 (2021) 87–109.
[16] G. Nie, Y. Dai, Y. Liu, J. Xie, S. Gong, N. Afzal, X. Zhang, L. Pan, J.-J. Zou, High yield one-pot synthesis of high density and low freezing point jet-fuel-ranged blending from bio-derived phenol and cyclopentanol, Chem. Eng. Sci. 207 (2019) 441–447.

[17] Z. Fang, X. Zhang, X. Zhuang, L. Ma, Recent advances in synthesis strategies for biomass-derived high-energy-density jet fuels, Renew. Sustain. Energy Rev. 202 (2024) 114715.
[18] X. Niu, R. Zhao, Y. Han, X. Zhang, Q. Wang, Highly dispersed platinum clusters anchored on hollow ZSM-5 zeolite for deep hydrogenation of polycyclic aromatic hydrocarbons, Fuel 326 (2022) 125021.
[19] N.N. Petrukhina, M.A. Vinnikova, A.L. Maksimov, Production of high-density jet and diesel fuels by hydrogenation of highly aromatic fractions, Russ. J. Appl. Chem. 91 (2018) 1223–1254.
[20] K. Cheng, Y. Li, J. Kang, Q. Zhang, Y. Wang, Selectivity control by relay catalysis in CO and CO_2 hydrogenation to multicarbon compounds, Acc. Chem. Res. 57 (2024) 714–725.
[21] K. Bing Tan, K. Xu, D. Cai, J. Huang, G. Zhan, Rational design of bifunctional catalysts with proper integration manners for CO and CO_2 hydrogenation into value-added products: a review, Chem. Eng. J. 463 (2023) 142262.
[22] A. Velty, A. Corma, Advanced zeolite and ordered mesoporous silica-based catalysts for the conversion of CO_2 to chemicals and fuels, Chem. Soc. Rev. 52 (2023) 1773–1946.
[23] Y. Li, X. Li, H. Zhang, J. He, K. Su, T. Chen, R. Zhang, H. Xu, Y. Wu, W. Yang, L. Liu, Tuning the spatial distribution and chemical nature of acid sites in MCM-22 zeolite by atomically dispersed lanthanum species for alkylation of 2-methylnaphthalene, ACS Catal. 115 (2024) 623–638.
[24] Z. Feng, C. Tang, P. Zhang, K. Li, G. Li, J. Wang, Z. Feng, C. Li, Asymmetric sites on the $ZnZrO_x$ catalyst for promoting Formate formation and transformation in CO_2 hydrogenation, J. Am. Chem. Soc. 145 (2023) 12663–12672.
[25] T. Liu, Z. Liu, S. Jiang, P. Peng, Z. Liu, A.D. Chowdhury, G. Liu, Selectivity control by zeolites during methanol-mediated CO_2 hydrogenation processes, Chem. Soc. Rev. 54 (2025) 2726–2761.
[26] S. Kattel, P.J. Ramírez, J.G. Chen, J.A. Rodriguez, P. Liu, Active sites for CO_2 hydrogenation to methanol on cu/ZnO catalysts, Science 355 (2017) 1296–1299.
[27] S.A. Ghafarian Nia, H. Shahbeik, A. Shafizadeh, S. Rafiee, H. Hosseinzadeh-Bandbafha, M. Kiehbadroudinezhad, S.A.F. Sheikh Ahmad Tajuddin, M. Tabatabaei, M. Aghbashlo, Machine learning-driven optimization for sustainable CO_2-to-methanol conversion through catalytic hydrogenation, Energ. Conver. Manage. 325 (2025) 119373.
[28] H. Wang, S. Fan, S. Guo, S. Wang, Z. Qin, M. Dong, H. Zhu, W. Fan, J. Wang, Selective conversion of CO_2 to isobutane-enriched C_4 alkanes over $InZrO_x$-Beta composite catalyst, Nat. Commun. 14 (2023) 2627.
[29] F. Sha, C. Tang, S. Tang, Q. Wang, Z. Han, J. Wang, C. Li, The promoting role of Ga in $ZnZrO_x$ solid solution catalyst for CO_2 hydrogenation to methanol, J. Catal. 404 (2021) 383–392.
[30] Y. Ren, H. Xiao, B. Chong, M. Xia, S. Kou, A. Xu, J. Li, J. Liu, H. Ou, Z. Ren, G. Yang, Constructing Mo^{5+} sites in molybdenum oxide by lattice stress for efficient ammonia synthesis, Applied Catalysis B: Environment and Energy 353 (2024) 124066.
[31] E. Caldeweyher, C. Bannwarth, S. Grimme, Extension of the D3 dispersion coefficient model, J. Chem. Phys. 147 (2017).
[32] E. Caldeweyher, S. Ehlert, A. Hansen, H. Neugebauer, S. Spicher, C. Bannwarth, S. Grimme, A generally applicable atomic-charge dependent London dispersion correction, J. Chem. Phys. 150 (2019).
[33] E. Caldeweyher, J.-M. Mewes, S. Ehlert, S. Grimme, Extension and evaluation of the D4 London-dispersion model for periodic systems, Phys. Chem. Chem. Phys. 22 (2020) 8499–8512.
[34] J. Wang, G. Li, Z. Li, C. Tang, Z. Feng, H. An, H. Liu, T. Liu, C. Li, A highly selective and stable ZnO-ZrO_2 solid solution catalyst for CO_2 hydrogenation to methanol, Sci. Adv. 3 (2017) e1701290.
[35] V. Wang, N. Xu, J.-C. Liu, G. Tang, W.-T. Geng, VASPKIT: a user-friendly interface facilitating high-throughput computing and analysis using VASP code, Comput. Phys. Commun. 267 (2021) 108033.
[36] K.J. Johnson, R.E. Morris, S.L. Rose-Pehrsson, Evaluating the predictive powers of spectroscopy and chromatography for fuel quality assessment, Energy Fuel 20 (2006) 727–733.
[37] J. Xie, T. Jia, S. Gong, N. Liu, G. Nie, L. Pan, X. Zhang, J.-J. Zou, Synthesis and thermal stability of dimethyl adamantanes as high-density and high-thermal-stability fuels, Fuel 260 (2020) 116424.
[38] X. Zhang, X. Yu, R.G. Mendes, P. Matvija, A.E.M. Melcherts, C. Sun, X. Ye, B. M. Weckhuysen, M. Monai, Highly dispersed ZnO sites in a ZnO/ZrO_2 catalyst promote carbon dioxide-to-methanol conversion, Angew. Chem. Int. Ed. 64 (2025) e202416899.
[39] B. Hong, X. Wang, Y. Lai, S. Huang, J. Liu, Q. Jiang, W. Zhou, Z. Yang, L. Ye, J. Zuo, G. Fu, Y. Yuan, Low-pressure CO_2 hydrogenation coupled with toluene methylation to *para*-xylene using atomic Pd-doped $ZnZrO_x$–HZSM-5, Applied Catalysis B: Environment and Energy 361 (2025) 124606.
[40] J. Zuo, W. Chen, J. Liu, X. Duan, L. Ye, Y. Yuan, Selective methylation of toluene using CO_2 and H_2 to *Para*-xylene, Sci. Adv. 6 (2020) eaba5433.
[41] X. Shang, H. Zhuo, Q. Han, X. Yang, G. Hou, G. Liu, X. Su, Y. Huang, T. Zhang, Xylene synthesis through tandem CO_2 hydrogenation and toluene methylation over a composite ZnZrO zeolite catalyst, Angew. Chem. Int. Ed. 62 (2023) e202309377.
[42] Y. Li, K. He, S. Zhao, L. Jiao, H. Chen, X. Ma, C. Dai, Highly selective production of 2-methylnaphthalene by CO_2 hydrogenation and naphthalene alkylation, Chem. Eng. J. 501 (2024) 157839.
[43] W. Zhang, S. Wang, S. Guo, Z. Qin, M. Dong, J. Wang, W. Fan, Effective conversion of CO_2 into light olefins over a bifunctional catalyst consisting of La-modified $ZnZrO_x$ oxide and acidic zeolite, Catal. Sci. Technol. 12 (2022) 2566–2577.
[44] S. Badoga, R.V. Sharma, A.K. Dalai, J. Adjaye, Hydrotreating of heavy gas oil on mesoporous zirconia supported NiMo catalyst with EDTA, Fuel 128 (2014) 30–38.
[45] J. Wang, S. Li, W. Liu, Y. Xiao, Z. Feng, X. Liang, S. Tang, G. Li, C. Dong, F. Pan, C. Li, The synergetic effect of dual active sites in ZnO-ZrO_2 catalyst for CO_2 hydrogenation to methanol, CCS Chemistry 6 (2024) 2996–3007.
[46] S. Chen, J. Wang, Z. Feng, Y. Jiang, H. Hu, Y. Qu, S. Tang, Z. Li, J. Liu, J. Wang, C. Li, Hydrogenation of CO_2 to light olefins over $ZnZrO_x$/SSZ-13, Angew. Chem. Int. Ed. 63 (2024) e202316874.
[47] R. Cao, T. Fu, Y. Liu, W. Qin, Y. Guo, C. Li, S. Huang, Z. Li, Boosting benzene alkylation conversion with CO_2/H_2 via a triple composite catalyst, ACS Catalysis 14 (2024) 12016–12030.
[48] A.S. Mokrushin, I.A. Nagornov, T.L. Simonenko, N.P. Simonenko, P.Yu. Gorobtsov, I.A. Arkhipushkin, E.P. Simonenko, V.G. Sevastyanov, N.T. Kuznetsov, Gas-sensitive nanostructured ZnO films praseodymium and europium doped: electrical conductivity, selectivity, influence of UV irradiation and humidity, Appl. Surf. Sci. 589 (2022) 152974.
[49] M. Thommes, K. Kaneko, A.V. Neimark, J.P. Olivier, F. Rodriguez-Reinoso, J. Rouquerol, K.S.W. Sing, Physisorption of gases, with special reference to the evaluation of surface area and pore size distribution (IUPAC technical report), Pure Appl. Chem. 87 (2015) 1051–1069.
[50] F. Sha, S. Tang, C. Tang, Z. Feng, J. Wang, C. Li, The role of surface hydroxyls on $ZnZrO_x$ solid solution catalyst in CO_2 hydrogenation to methanol, Chin. J. Catal. 45 (2023) 162–173.
[51] M.-J. Xi, X.-Y. Yu, X. Su, L. Xiong, X. Ning, P. Gao, Z.-Q. Huang, C.-R. Chang, Uncovering the crucial role of oxygen vacancy in altering activity and selectivity of CO_2 hydrogenation on $ZnGa_2O_4$ spinel surfaces, ACS Catalysis 15 (2025) 4185–4197.
[52] Y. Li, Y. Ren, G. Yang, L. Wang, Unraveling the role of $ZnZrO_x$ morphology and oxygen vacancy in bifunctional catalyst for conversion of syngas into light olefins, Applied Catalysis B: Environment and Energy 365 (2025) 124945.
[53] F. Zhang, B. Li, X. Quan, K. Wang, J. Xu, T. Wu, Z. Li, M. Yan, S. Liu, Y. He, Y. Shi, Y. Su, P. Xie, Revealing the dynamics of oxygen vacancy in ZnO_{1-x}/cu during robust methanol synthesis from CO_2, ACS Catalysis 14 (2024) 7136–7148.
[54] H. Tian, Z. Chen, H. Huang, F. Zha, Y. Chang, H. Chen, Hydrogenation of CO_2 to p-xylene over $ZnZrO_x$/hollow tubular HZSM-5 tandem catalyst, J. Energy Chem. 99 (2024) 725–737.
[55] S. Ahmed, J.R. Sugiarto, W. Yoon, M. Irshad, H. Jo, S.S. Bibi, S.K. Kim, M.K. Khan, J. Kim, High-yield pentanes-plus production via hydrogenation of carbon dioxide: revealing new roles of zirconia as promoter of iron catalyst with long-term stability, J. Energy Chem. 102 (2025) 431–442.
[56] Y. Wang, S. Kattel, W. Gao, K. Li, P. Liu, J.G. Chen, H. Wang, Exploring the ternary interactions in cu–ZnO–ZrO_2 catalysts for efficient CO_2 hydrogenation to methanol, Nat. Commun. 10 (2019) 1166.
[57] Y. Zhao, P. Shi, X. Wang, X. Guo, R. Yao, Y. Li, Q. Jia, H. Ban, L. Li, C. Li, Electronic interaction promoting CO_2 hydrogenation to light olefins over $ZnZrO_x$/SAPO-34 catalyst, Chem. Eng. J. 503 (2025) 158350.
[58] Y. Wei, Y. Li, Y. Xu, Y. Zu, Y. Sun, T. Xu, H. Liang, J. Bai, Synergy of oxygen vacancies and surface Zn in tuned ZnO crystal facets for enhanced CO_2 cycloaddition to epoxides, Applied Catalysis B: Environment and Energy 365 (2025) 124878.
[59] Y. Wang, S. Liu, F. Liu, M. Yao, J. Ma, S. Geng, J. Cao, X. Wang, Effective synergistic interaction between $InZnZrO_x$ ternary metal oxides and SAPO-34 molecular sieve catalysts for CO_2 hydrogenation to light olefins, Chem. Eng. J. 500 (2024) 157398.
[60] X. Wang, Z. Yao, X. Guo, Z. Yan, H. Ban, P. Wang, R. Yao, L. Li, C. Li, Modulating electronic interaction over Zr–ZnO catalysts to enhance CO_2 hydrogenation to methanol, ACS Catal. (2023) 508–521.
[61] H. Zhao, R. Yu, S. Ma, K. Xu, Y. Chen, K. Jiang, Y. Fang, C. Zhu, X. Liu, Y. Tang, L. Wu, Y. Wu, Q. Jiang, P. He, Z. Liu, L. Tan, The role of Cu_1–O_3 species in single-atom Cu/ZrO_2 catalyst for CO_2 hydrogenation, Nat. Catal. 5 (2022) 818–831.
[62] H. Tian, C. Jiao, Q. Li, Z. Chen, H. Huang, F. Zha, X. Guo, X. Tang, H. Chen, Catalytic hydrogenation of CO_2 to aromatics over indium-zirconium solid solution and sheet HZSM-5 tandem catalysts, Appl. Surf. Sci. 678 (2024) 161155.
[63] X. Shang, Q. Han, W. Zhang, Y. Wei, G. Liu, G. Hou, X. Su, Y. Huang, T. Zhang, Methoxy-bridged tandem CO_2 hydrogenation and ethylbenzene alkylation for selective synthesis of *para*-ethyl-toluene, Applied Catalysis B: Environment and Energy 348 (2024) 123833.
[64] X. Jiang, X. Nie, X. Guo, C. Song, J.G. Chen, Recent advances in carbon dioxide hydrogenation to methanol via heterogeneous catalysis, Chem. Rev. 120 (2020) 7984–8034.
[65] Z. Tang, S. Zhao, X. Zhao, R. Jin, J. Wang, Z. Zhang, H. Hu, X. Guo, C. Dai, X. Ma, "ZnAlCrO_x&HZSM-5" bifunctional catalyst for one-step alkylation of naphthalene and syngas, Fuel 332 (2023) 126093.
[66] T. Pinheiro Araújo, J. Morales-Vidal, T. Zou, M. Agrachev, S. Verstraeten, P. O. Willi, R.N. Grass, G. Jeschke, S. Mitchell, N. López, J. Pérez-Ramírez, Design of Flame-Made $ZnZrO_x$ catalysts for sustainable methanol synthesis from CO_2, Adv. Energy Mater. 13 (2023) 2204122.
[67] W. Wang, Y. Liu, C. Shi, L. Pan, X. Zhang, J.-J. Zou, High energy density renewable fuels based on multicyclic sesquiterpene: synthesis and performance, Fuel 318 (2022) 123665.
[68] J. Xie, H. Zhang, T. Jia, J. Xie, J.-J. Zou, Synthesis and fuel properties of high-density and low-freezing-point asymmetric cycloalkyl adamantane, Fuel Process. Technol. 244 (2023) 107707.
[69] R. Hubesch, M. Mazur, P.R. Selvakannan, K. Föger, A.F. Lee, K. Wilson, S. Bhargava, Endothermic catalytic cracking of liquid hydrocarbons for thermal management of high-speed flight vehicles, Sustainable Energy Fuels 6 (2022) 1664–1686.